ELSEVIER

Research paper

Generalized thermodynamic modeling of hydrogen storage tanks for truck application

Laura Stops *, Daniel Siebe, Alexander Stary, Johannes Hamacher, Valeria Sidarava, Sebastian Rehfeldt, Harald Klein

Technical University of Munich, TUM School of Engineering and Design, Department of Energy and Process Engineering, Institute of Plant and Process Technology, 85748 Garching, Germany

ARTICLE INFO

ABSTRACT

Hydrogen-driven heavy-duty trucks are a promising technology for reducing CO_2 emissions in the transportation sector. Thus, storing hydrogen efficiently onboard is vital. The three available or currently developed physical hydrogen storage technologies (compressed gaseous, subcooled liquid, and cryo-compressed hydrogen) are promising solutions. For a profound thermodynamic comparison of these storage systems, a universally applicable model is required. Thus, this article introduces a generalized thermodynamic model and conducts thermodynamic comparisons in terms of typical drive cycle scenarios. Therefore, a model introduced by Hamacher et al. [1] for cryo-compressed hydrogen tanks is generalized by means of an explicit model formulation using the property c_{v2P} from REFPROP [2], which is understood as a generic specific isochoric two-phase heat capacity. Due to an implemented decision logic, minor changes to the equation system are automatically made whenever the operation mode or phase of the tank changes. The resulting model can simulate all three storage tank systems in all operating scenarios and conditions in the single- and two-phase region. Additionally, the explicit model formulation provides deeper insights into the thermodynamic processes in the tank. The model is applied to the three physical hydrogen storage technologies to compare drive cycles, heat requirement, dormancy behavior, and optimal usable density. The highest driving ranges were achieved with cryo-compressed hydrogen, however, it also comes with higher heating requirements compared to subcooled liquid hydrogen.

Contents

---

* Corresponding author.
   E-mail address: laura.stops@tum.de (L. Stops).

Nomenclature

Symbols

A	Area	m^2
c_p	Specific isobaric heat capacity	J/(kg K)
c_v	Specific isochoric heat capacity	J/(kg K)
c_{v2P}	Specific isochoric two-phase heat capacity	J/(kg K)
h	Specific enthalpy	J/kg
k	Heat transfer coefficient	W/(m^2 K)
M	Mass	kg
$\dot{M}$	Mass flow	kg/s
p	Pressure	Pa
$\dot{Q}$	Heat flow	W/s
R	Specific gas constant	J/(K kg)
s	Specific entropy	J/kg
T	Temperature	K
t	Time	s
U	Internal energy	J
u	Specific internal energy	J/kg
V	Volume	m^3
v	Specific volume	m^3/kg
x	Vapor fraction	-
ϱ	Density	kg/m^3

Sub- and superscripts

$'$	Saturated liquid
$''$	Saturated gas
alu	Aluminum
amb	Ambient
cf	Carbon fiber
disch	Discharge
fill	Filling
fuel	Refueling
i	Inner
min	Minimum
o	Outer
s	Solid
sat	Saturation
stop	Stop
tank	Tank
use	Usable
vent	Venting

Abbreviations

BEV	Battery Electric Vehicle
FCEV	Fuel Cell Electric Vehicle
FC	Fuel Cell
CcH2	Cryo-Compressed Hydrogen
LH2	Liquid Hydrogen
LOHC	Liquid Organic Hydrogen Carrier
sLH2	Subcooled Liquid Hydrogen
CH2	Compressed Gaseous Hydrogen

DAE	Differential-Algebraic System of Equations
MLI	Multi-Layer Insulation

1. Introduction

To encounter the disruptive challenges of climate change, several national and international agreements, such as the European Green Deal or the Paris Agreement, have been released in the last decades to limit CO_2 emissions and global warming [3–5]. To meet the declared goals, also the CO_2 emissions in the transport sector need to be reduced tremendously. Thereby, hydrogen is one key energy source for CO_2-emission-free drive trains, e.g., when it is used to feed a Fuel Cell (FC) which generates energy for electric motors. Thus, there is a current research focus on hydrogen-powered cars, ships, or aircraft [6–9]. As such, Fuel Cell Electric Vehicles (FCEVs) are already commercially available for the passenger car sector [10,11] and first hydrogen-driven ships have been released [12]. Also in the aviation sector, hydrogen-fueled planes are currently being developed, e.g., by ZeroAvia [13] and Airbus [14]. However, in this paper the focus is on the application of hydrogen in the heavy-duty truck sector.

With a share of approximately 26 % of the overall CO_2 emissions within the EU in 2020, road transportation is one of the largest emitters [15]. Thereby, heavy-duty trucks and buses are responsible for approximately 28 % of the transportation emissions and are thus prone to cut overall emissions. Whereas Battery Electric Vehicles (BEVs) are communicated as the most significant future technology in the passenger car market by car manufacturers [16–18], they show disadvantages regarding payload and charging times when applied to long-range or high-utilization transportation applications like heavy-duty trucks [19,20]. In contrast, FCEVs are characterized by high driving ranges (more than 500 km [19]) and significantly faster refueling (approximately 10 min to 15 min [21,22]). Thus, FCEVs are a promising CO_2-emission-free alternative in the heavy-duty truck sector [18,19] and are therefore suggested for these applications by the German government as part of the National Hydrogen Strategy [23]. Currently, the first commercial hydrogen-driven trucks are already available and further prototypes are being developed [24–26].

For efficient use of hydrogen in high-utilization heavy-duty applications, a long range resulting from a high storage density, quick refueling, and loss-free operation are vital. Thus, ways of storing hydrogen efficiently onboard a truck need to be investigated. Several reviews [27–29] summarize and compare different hydrogen storage systems. Hassan et al. [27] assign storage systems either to physical methods (Compressed Gaseous Hydrogen (CH2), Liquid Hydrogen (LH2), and Cryo-Compressed Hydrogen (CcH2)) or material-based methods. The latter include adsorptive materials, metal hybrids, or chemical storage materials, such as Liquid Organic Hydrogen Carriers (LOHCs). These technologies show potential in handling and transportation. How-
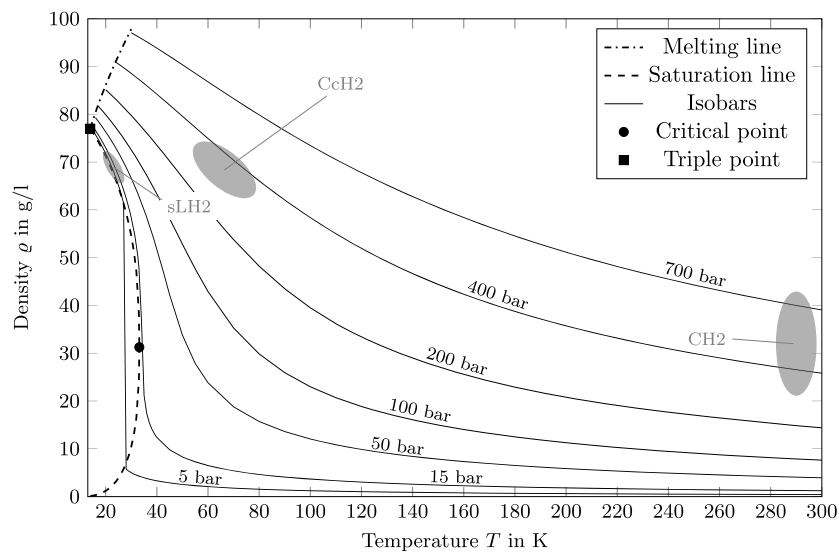
Fig. 1. Thermodynamic states of different physical hydrogen storage technologies in a temperature-density diagram of normal hydrogen [1,31].

ever, they are limited in the storage density, costs, or operating conditions [27] and are not further considered in this paper.

In Fig. 1, the three physical methods are depicted within a temperature-density diagram, showing the thermodynamic states at full tank conditions, using the thermodynamic data of normal hydrogen.[1] The diagram shows a large density and temperature range, going from cryogenic to ambient temperatures. Furthermore, isobars, the critical and triple point, and the saturation and melting lines are shown. Further, it must be noted that instead of LH2, Subcooled Liquid Hydrogen (sLH2) is depicted. sLH2 is LH2 stored above the critical pressure at subcooled liquid conditions. In this paper, sLH2 is considered for investigation instead of LH2 since the technology offers advantages, such as higher storage densities and avoiding hydrogen losses during refueling. Thus, it is currently being investigated by truck manufacturers [25].

It can be seen that the highest storage densities are reached with CcH2, where hydrogen is stored at high pressure and low temperature. sLH2 is stored at even lower temperatures and low pressure close to the two-phase region and is also characterized by high storage densities. CH2, on the other hand, is stored at high pressure and ambient temperatures and has the lowest storage density.

To further describe the aggregate phases of hydrogen, Fig. 2 shows the saturation line in a temperature-pressure diagram. The saturation line marks the vapor-liquid equilibrium and corresponds to the two-phase region in the temperature-density diagram in Fig. 1. Above the critical point, no distinction between the phases is possible. Thus, above the critical temperature of 33.15 K and the critical pressure of 12.96 bar (for normal hydrogen) [30], the hydrogen is in the supercritical phase. For para hydrogen, which is considered for CcH2 and sLH2 in this paper, the critical point is at 32.94 K and 12.86 bar. When comparing the value range to the physical storage technologies shown in the temperature-density diagram in Fig. 1, it can be observed that CcH2 and CH2 are actually in the supercritical area. Instead, sLH2 is typically stored at temperatures below the critical temperature and is thus in the subcooled liquid or two-phase region.

Due to the different operating ranges of the three physical storage technologies, different requirements result for the solid storage tanks. The tanks are typically divided into four categories [29]. Type I tanks
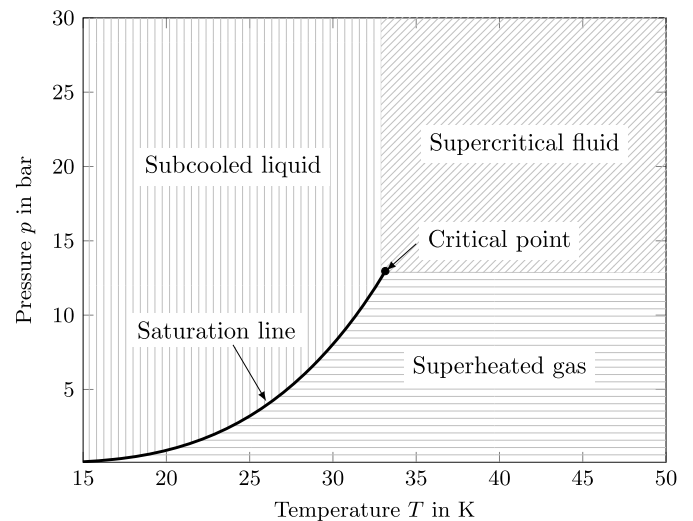

Fig. 2. Saturation line and state of matters of normal hydrogen in a temperature-pressure diagram.

are made of steel only and can hold up to 300 bar pressures. Type II tanks are composed of steel wrapped with carbon fiber-reinforced plastics to decrease the overall tank weight. Type III tanks are made out of a steel or aluminum liner inside a carbon or glass fiber-reinforced plastic cylinder, allowing for higher pressures. Finally, type IV tanks differ from type III tanks by the liner, which is made out of a polymer, resulting in a lighter tank that can withstand up to 700 bar.

The current state-of-the-art hydrogen storage onboard trucks is CH2 in high-pressure vessels at ambient temperature and 350 bar to 700 bar pressure [32], shown on the right side of Fig. 1. Therefore, typically type III or type IV tanks are used [33]. Depending on the pressure, the maximum hydrogen density in such tanks lies between 23 g/L to 40 g/L [2]. Despite this comparably low storage density [6,32] and high requirement for expensive carbon fiber [34], CH2 systems are already applied in commercial FCEV trucks, e.g., distributed by Hyundai [24]. However, with a storage capacity of approximately 32 kg hydrogen at a tank pressure of 350 bar [24], the driving range of these trucks is significantly lower compared to conventional diesel trucks and insufficient for long-range applications.

One solution with higher storage density and, thus, longer driving ranges is LH2 or sLH2, where hydrogen is stored at cryogenic temper-

---

[1] As hydrogen molecules consist of two hydrogen nuclei, there are two forms of hydrogen related to the quantum states. The first type, where the two nucleus spins are parallel, is called ortho hydrogen, whereas the other is called para hydrogen. Depending on the temperature, an equilibrium composition is established, which is referred to as normal hydrogen [30].

atures (20 K to 30 K) and low pressure [32]. Therefore, double-walled, vacuum-insulated, and low-pressure vessels [35] are applied. With this technology, fill densities of 70.9 g/L can be reached [27]. However, storing the hydrogen in liquid form requires high insulation effort since such storage systems commonly suffer from evaporation losses due to heat entry [32]. Studies for applying LH2 in the passenger car application have already been conducted in the past, typically assuming a tank composed of a metal liner, vacuum, and insulation foils [36]. Currently, LH2 and sLH2 solutions are being developed for the heavy-duty truck sector. As such, Daimler Truck has recently presented a prototype [25].

The highest storage density of all physical methods is reached with CcH2 [31,37,38]. Thereby, hydrogen is stored supercritically in type III tanks [39]. In studies considering the passenger car sector, operating pressures of 20 bar to 350 bar and temperatures of 33 K to 233 K were suggested [31]. The technology was introduced by Aceves et al. [40] and shows the longest driving range with one tank [41]. Furthermore, less hydrogen is lost due to venting compared to LH2 [31,40,41], and CcH2 tanks require less expensive carbon fiber material compared to CH2 [42]. Consequently, CcH2 is a promising technology for CO_2-emission-free trucks. As the CcH2 concept has already been studied and tested for the car domain [42], the knowledge is currently transferred and adapted to develop CcH2 heavy-duty trucks [26].

Regardless of the tank type, multiple other components, such as valves or sensors, are included in the overall tank system. In contrast to the CH2 tank, the sLH2 and the CcH2 require two heat exchangers to control hydrogen pressure and temperature [31,36]. One heat exchanger is required to heat the hydrogen provided to the FC since FCs are typically operated at temperatures above 60 °C [6]. Hereafter, it is referred to as the outer heat exchanger. The second heat exchanger, here referred to as the internal heat exchanger, adds heat to the tank for ensuring a certain minimum pressure in the hydrogen tank [31,36,43]. Therefore, warm hydrogen can be recirculated through the internal heat exchanger [31,43].

The development of a reliable onboard hydrogen storage system for all three physical storage systems also requires dynamic modeling of the tank as well as the complete truck system for accurate prediction of the thermodynamic state of the stored hydrogen. Therefore, all operating scenarios of the truck must be thoroughly investigated, including driving, where hydrogen is discharged from the tank, as well as refueling and dormancy. Several approaches to simulate these aspects based on energy and mass balances can be found in the literature. For instance, Aceves et al. [40] published a simple model for calculating hydrogen losses in a CcH2 car tank due to venting. Ahluwalia and Peng [43] later developed a more advanced dynamic model to characterize CcH2 storages for car applications in all three operating scenarios, using separate models for each scenario. Furthermore, in each mode, they employ distinct models for the single-phase and two-phase regions. In the latter one, liquid and gaseous hydrogen are balanced separately. These models were also applied to LH2 cars by changing the starting conditions of the simulations. Ahluwalia et al. [44] further extended their research by adding cost models for a comprehensive assessment of CcH2 tanks, while Peng and Ahluwalia [45] also considered the conversion of para to ortho hydrogen, which primarily impacts dormancy. The results of these simulation models were also verified experimentally [41,42].

More recently, Ahluwalia et al. [46] adjusted their model to simulate CcH2 buses, therefore only considering single-phase operation. Again, the simulation model uses separate equation systems for refueling, discharge, and dormancy, and also accounts for the conversion of para to ortho hydrogen. Moreno-Blanco et al. [47] used a similar model for single-phase car applications, focusing on the conversion of para to ortho hydrogen and its influence on dormancy, fill density, and drive cycles.

Based on their previous publications, Ahluwalia et al. [48] also developed a thermodynamic model of an LH2 tank for heavy-duty trucks, where hydrogen is stored at saturation conditions. Thereby, hydrogen is considered a mixture of liquid and gaseous hydrogen in phase equilibrium. The model is used to study different driving scenarios and to calculate the usable density of the tank.

In a recent paper by Hamacher et al. [1], a novel implicit model formulation of a CcH2 tank for heavy-duty truck applications was derived. This formulation employs a single set of differential-algebraic equations to describe all three operational scenarios. Only three equations are switched automatically depending on the operational mode. The model's capabilities are demonstrated by simulations of characteristic drive cycles. However, due to its implicit nature, the model equations themselves provide little insight into the thermodynamics, e.g., the temperature change characteristics. Additionally, the partial derivatives used in the equation system are not defined for two-phase operations.

To address these limitations, this paper presents a further developed and generalized explicit model formulation based on the model of Hamacher et al. [1]. This new formulation offers more insights into the thermodynamic processes. Furthermore, by utilizing a "specific isochoric two-phase heat capacity" property from REFPROP [2], the model also allows the simulation of all operation modes within the two-phase system. To accomplish this, the model requires switching some equations depending on the tank conditions. Thus, a logical algorithm is presented to automatically switch between different model formulations. The resulting model including the logical equation-switch system now allows to calculate all kinds of physical hydrogen storage tanks in all operating conditions, thus also allowing to compare the storage technologies and derive desirable drive cycle strategies. Furthermore, in the appendix, detailed derivations of the equations in the single- and two-phase region and proper documentation of the calculation of the specific isochoric two-phase heat capacity c_{v2P} are provided.

Hereafter, the paper is structured as follows. First, a generalized explicit hydrogen tank model formulation is derived and analyzed in Section 2, based on the implicit CcH2 model by Hamacher et al. [1]. Then, the model is applied to simulate and compare typical drive cycle studies for the three considered storage technologies, CH2, sLH2, and CcH2, in Section 3. Finally, a short summary is given in Section 4.

2. Methodology

The primary objective of this paper is to introduce an explicit thermodynamic model capable of accurately describing hydrogen truck tanks in all operation scenarios. In a prior publication, Hamacher et al. [1] developed an implicit model for CcH2 tanks used in truck applications. While the model is able to fully describe CcH2 and CH2 tanks, it cannot fully describe a sLH2 tank due to partial derivatives that are not defined in the two-phase region. Thus, the hereafter presented explicit model can be regarded as an advancement and generalization of the implicit model by Hamacher et al. [1] that is able to describe all relevant physical hydrogen storage tanks for truck application. Furthermore, the explicit model formulation affords a deeper understanding of the hydrogen thermodynamics, as the equations allow for advanced thermodynamic interpretation.

In addition to the explicit formulation, the model is further enhanced by departing from the assumption made by Hamacher et al. [1] that in the tank, solid and hydrogen temperatures are equal. Instead, natural convection between the solid and the hydrogen is considered to improve the model's accuracy.

2.1. Model overview

For the sake of simplicity, several assumptions that were made in Hamacher et al. [1], are also made similarly for the explicit tank model introduced in this paper.

- It is assumed that the hydrogen in the tank is perfectly mixed, resulting in uniform hydrogen temperature and pressure over the

whole tank. Even though temperature stratification has been observed in experimental studies [33], this is a common simplyfing assumption [1,37,40,43].

- For all CcH2 and sLH2 simulations, it is assumed that only para hydrogen is present, and no conversion of para to ortho hydrogen is considered. In the case of liquid hydrogen, the equilibrium composition is predominantly para hydrogen [6]. As all studies conducted in this paper assume refueling from liquid hydrogen for both CcH2 and sLH2, the assumption of pure para hydrogen is clearly justified right after refueling. Given the cryogenic temperatures during the primary phases of the considered drive cycles for CcH2 and sLH2, coupled with the slow kinetics of the para-ortho conversion process [49], we extend the assumption of pure para hydrogen to the entire range of consideration. While previous studies have shown the importance of the para-ortho conversion for dormancy in the passenger car sector [45,47], they have also shown that the influence decreases with increasing daily driving range. Thus, this justifies the assumption for the high-utilization application in this paper.
- For CH2 instead, the composition of normal hydrogen is assumed. This corresponds to the equilibrium composition of hydrogen, consisting of approximately 75 % ortho and 25 % para hydrogen at ambient temperatures.
- The thermodynamic properties of hydrogen are calculated using the database REFPROP [2] based on the equation of state by Leachman et al. [30].
- The temperature dependent specific heat capacities of aluminum c_{alu} and carbon fiber c_{cf} are calculated by data from NIST webbook [50,51].

Additionally, further assumptions are required for the generalized model as it includes extended two-phase operation and a separate solid energy balance.

- Since carbon fiber and aluminum are in direct thermal contact and both materials have a good thermal conductivity, it is assumed that both solid materials are at the same uniform temperature all the time. Thus, only one solid block temperature is considered.
- Only natural convection is considered between the hydrogen and the solid tank materials.
- Whenever hydrogen is present as a two-phase mixture, it is assumed to be in phase equilibrium. This is in contrast to stationary LH2 tanks, often described by non-equilibrium models in literature [52–54]. In the case of a moving tank, effects like sloshing are expected [35]. Given that sloshing promotes thorough mixing of the phases, the equilibrium assumption is more justified during discharge simulations. Furthermore, it is worth noting that all simulations in this paper, which pass through the two-phase region, start and end within the single-phase region, further supporting the assumption of phase equilibrium. Nevertheless, it must be considered that this assumption simplifies the model, allowing for a good overall description of tank behavior but overlooking the intricacies of phase interactions.

For modeling a typical hydrogen tank, different tank states need to be defined. First, there are three operating scenarios:

- **Discharge**: The truck is driving and hydrogen is discharged from the tank with the constant mass flow rate $\dot{M}_{disch}$. No hydrogen is vented or refueled.
- **Refueling**: The truck is refueled with the constant mass flow rate $\dot{M}_{fuel}$. No hydrogen is discharged or vented from the tank.
- **Dormancy**: The truck is standing and no hydrogen is fueled or discharged. When the pressure level has risen to a certain maximum system pressure p_{vent}, hydrogen is vented with the mass flow rate $\dot{M}_{vent}$ to keep the pressure at this maximum pressure p_{vent}.
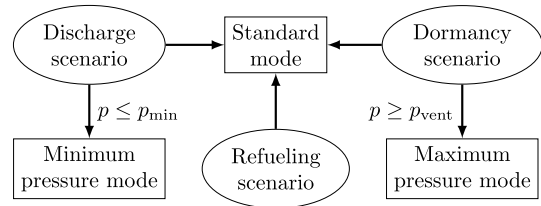

Fig. 3. Visualization of the relationship between the three operating scenarios and the three operational modes.

Furthermore, there are three operational modes that need to be differentiated:

- **A) Standard mode**: The pressure is within the operational boundaries ($p_{min} < p < p_{vent}$).
- **B) Minimum pressure mode**: The pressure is at the minimum system pressure ($p \leq p_{min}$). Heating of the tank is required to keep the pressure.
- **C) Maximum pressure mode**: The pressure is at the maximum system pressure ($p \geq p_{vent}$). Venting of hydrogen from the tank is required to keep the pressure.

Whereas the standard mode appears in all operating scenarios, the minimum pressure mode is only relevant for the discharge scenario, and the maximum pressure mode is only relevant for the dormancy operating scenario. Fig. 3 further clarifies the relationship between the three operating scenarios and operational modes. In the discharge and dormancy scenarios, the pressure level defines whether the tank is at standard, minimum, or maximum pressure mode. In contrast, in the refueling scenario, the tank is always in standard mode. However, here, an exception is made. The pressure in the tank may drop below the minimum pressure, as already shown in Hamacher et al. [1]. However, during refueling this is not critical as the final pressure after the refueling will always end up within the operational boundaries. Thus, there is no need to switch the operational mode and the internal heat exchanger is kept shut off.

Similar to the approach in Hamacher et al. [1], the distinction between the operational modes is important for deriving the required equation configuration for describing the thermodynamics in the tank. Whereas most equations are valid for all operational modes, some equations need to be switched, which results in three equation system configurations (A, B, and C) for the three operational modes. Since, in this paper, all modes should also be describable in the two-phase region for generalization of the model, the equations need to be adapted when the hydrogen enters or leaves the two-phase region. Therefore, another adapted form is derived for each configuration A, B, and C, as further explained in Section 2.3. The resulting logical structure of the overall model is visualized in Fig. 4.

The introduced model is implemented in MATLAB® R2022b, using the solver ode15s with automatic step size adaption. When starting a simulation, the equation system is first initialized for the corresponding operational mode at the starting conditions. Then, it is checked whether the hydrogen is at saturation pressure, which would then require the use of the two-phase configuration instead of the single-phase configuration. Regardless of which configuration is used, a solver step is performed. Within the solver routine, required operational mode changes are detected by a MATLAB® event function that compares the tank pressure to the minimum and maximum pressure, respectively. If an event is triggered, the solver is halted and the equation configuration is switched to B or C. Furthermore, the event function includes termination criteria that stop the simulation before a set end time is reached. These termination criteria depend on the operation scenario and the storage system and are further clarified in Section 3.

The modularization of the truck operation into three operational modes and three operating scenarios in combination with the imple-
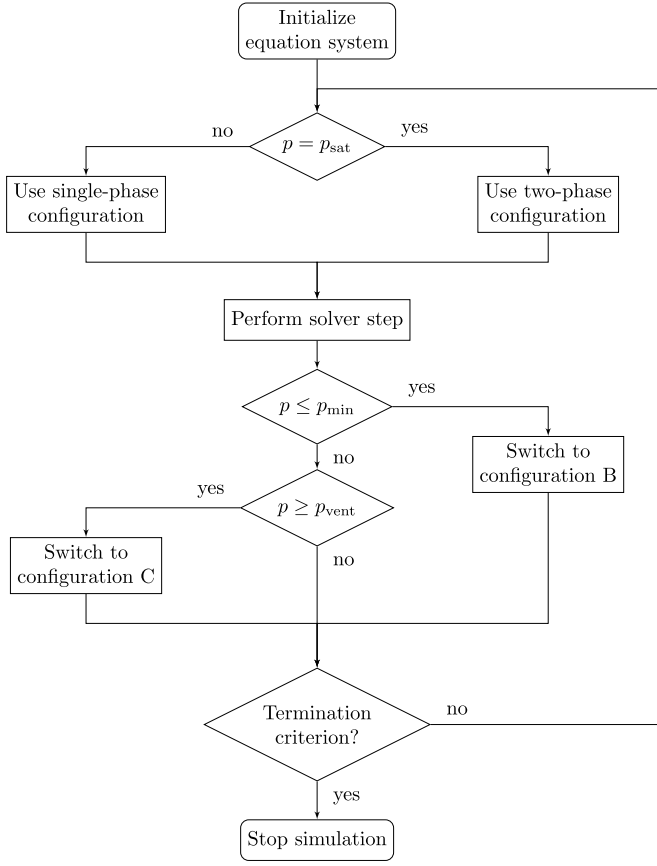
Fig. 4. Logical model structure.

mented decision logic brings high flexibility. As such, the model can easily be used for any investigations and optimizations of real-life drive cycles by defining them as a sequence of operating scenarios.

Similar to Hamacher et al. [1], a Differential-Algebraic System of Equations (DAE) is used to model the hydrogen tank. In addition to the mass and energy balance of the hydrogen and the energy balance of the solid tank material, seven algebraic equations are applied. In the following sections, the explicit differential equations for the three balances are derived and adapted for the two-phase region before the algebraic equations are discussed. For the sake of readability, the properties describing the hydrogen within the tank are written without an index in the following thermodynamic equations. Further, for describing processes in the two-phase region, the saturated liquid phase is declared with $'$ and the saturated vapor phase with $''$ in the following.

2.2. Differential equations

Fig. 5 illustrates the system boundaries for the solid and the hydrogen of the tank. Considering the hydrogen system on the left side, three mass flows are visible: the refueling mass flow $\dot{M}_{\text{fuel}}$ into the tank, the discharge mass flow $\dot{M}_{\text{disch}}$, and the venting mass flow $\dot{M}_{\text{vent}}$ out of the tank. Each mass flow only appears in one of the previously described operation scenarios and becomes zero in the other cases. Whereas $\dot{M}_{\text{disch}}$ and $\dot{M}_{\text{fuel}}$ are assumed to be constant parameters, $\dot{M}_{\text{vent}}$ needs to be determined by the equation system. By balancing the hydrogen mass M, the first differential equation is formulated as follows:

$$\frac{\mathrm{d}M}{\mathrm{d}t} = \dot{M}_{\text{fuel}} - \dot{M}_{\text{disch}} - \dot{M}_{\text{vent}} \ . \tag{1}$$

Additionally to the mass flows, two heat flows are shown on the left side of Fig. 5. Thereby, $\dot{Q}_{\text{s}}$ is the heat flow between the solid tank material and the hydrogen in the tank. The second heat flow $\dot{Q}_{\text{disch}}$ occurs

between an internal heat exchanger and the hydrogen. It is required to keep a minimum pressure during discharge when the tank is at the minimum pressure operational mode. From the shown mass and heat flows, the following general energy balance for the internal energy U of the hydrogen can be derived:

$$\frac{\mathrm{d}U}{\mathrm{d}t} = \dot{M}_{\text{fuel}} \cdot h_{\text{fuel}} - \dot{M}_{\text{disch}} \cdot h_{\text{disch}} - \dot{M}_{\text{vent}} \cdot h_{\text{vent}} + \dot{Q}_{\text{s}} + \dot{Q}_{\text{disch}} \ . \tag{2}$$

In Equation (2), h_{fuel}, h_{disch}, and h_{vent}, are the specific enthalpies corresponding to the mass flows for refueling, discharge, and venting. In contrast to Hamacher et al. [1], where it is assumed that all streams leaving the tank are at the same thermodynamic state as the ideally mixed tank, here, a distinction is made between single-phase and two-phase operations. In a hydrogen tank in two-phase state, it is unlikely that a stream with the equilibrium composition of vapor and liquid is extracted. Thus, it is assumed that in both scenarios, where hydrogen is withdrawn from the tank (discharge and venting), a single-phase stream is always extracted. Therefore, the specific enthalpy h of the extracted stream (h_{disch} or h_{vent}) needs to be defined. For single-phase operation, still an ideal mixture is assumed, thus h_{disch} and h_{vent} both equal h. However, when the hydrogen is in the two-phase region, it is assumed that only saturated gaseous hydrogen is vented ($h_{\text{vent}} = h''$). During driving, the hydrogen could be either discharged as a liquid ($h_{\text{disch}} = h'$) by extracting at the bottom of the tank, or as vapor ($h_{\text{disch}} = h''$) by extracting at the top of the tank. Both discharge setups can be simulated by the model, however in this paper, discharging saturated liquid hydrogen is assumed as base case. Later in the results (Section 3), this base case will be compared to the discharge of saturated vapor.

Equation (3) and Equation (4) summarize the definition of the enthalpies of the extracted streams depending on the hydrogen phase and, thus, on whether the pressure p equals the saturation pressure p_{sat}:

$$h_{\text{disch}} = \begin{cases} h' \text{ or } h'' & \text{if } p(T) = p_{\text{sat}}(T) \\ h & \text{otherwise} \end{cases} \tag{3}$$

$$h_{\text{vent}} = \begin{cases} h'' & \text{if } p(T) = p_{\text{sat}}(T) \\ h & \text{otherwise} \ . \end{cases} \tag{4}$$

Venting saturated vapor in the two-phase region comes with an energetic advantage: During dormancy, where as little hydrogen as possible should be vented, the more energetic phase is vented, keeping the total mass loss small. During discharge, however, the hydrogen temperature is decreased when mass is withdrawn from the tank, resulting in an enhanced pressure decrease (see further in Section 3). Consequently, the tank needs to be heated to keep a minimum pressure. By discharging the less energetic liquid phase in the base case, the amount of heat that needs to be added to the hydrogen is kept lower.

The specific enthalpy h_{fuel} of the refueling hydrogen mass flow results from a simplified refueling station model and will be further discussed in Section 2.5

While in Equation (2) the temperature T of the hydrogen could be calculated implicitly, as shown in Hamacher et al. [1], an explicit formulation is used in this paper. Therefore, the second explicit differential equation (Equation (5)) is derived by reformulating Equation (2) to an explicit equation for the temperature T:

$$\begin{aligned} M \cdot c_v \cdot \frac{\mathrm{d}T}{\mathrm{d}t} =& \dot{M}_{\text{fuel}} \cdot \left(h_{\text{fuel}} - h \right) \\ & - \dot{M}_{\text{vent}} \cdot \left(h_{\text{vent}} - h \right) \\ & - \dot{M}_{\text{disch}} \cdot \left(h_{\text{disch}} - h \right) \\ & + \frac{T}{\varrho} \cdot \left(\frac{\partial p}{\partial T} \right)_\varrho \cdot \left(\dot{M}_{\text{fuel}} - \dot{M}_{\text{disch}} - \dot{M}_{\text{vent}} \right) \\ & + \dot{Q}_{\text{s}} + \dot{Q}_{\text{disch}} \ . \end{aligned} \tag{5}$$

A detailed documentation of the derivation is given in Appendix A.1. In Equation (5), c_v is the specific isochoric heat capacity, h is the specific enthalpy, and ϱ is the density of the ideally mixed hydrogen in

(a) Hydrogen system control volume
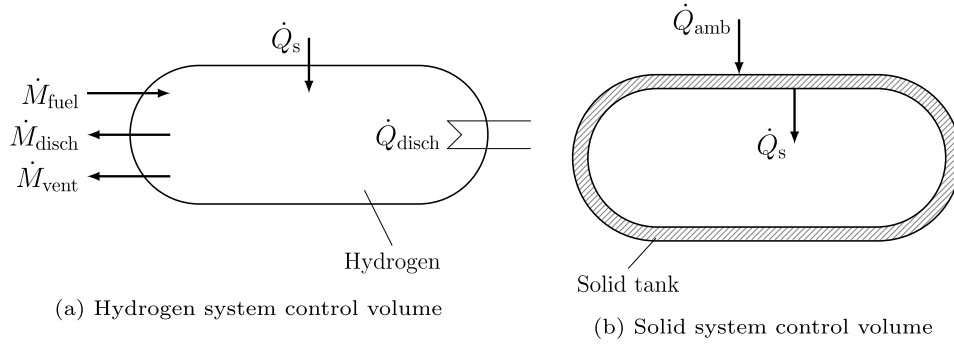
(b) Solid system control volume

Fig. 5. System control volumes of hydrogen and the solid tank.

the tank. Compared to the implicit equation Equation (2), Equation (5) gives better insight into the thermodynamic processes in the tank. The first three lines show the effect of the enthalpy streams on the temperature T. Thereby, not the absolute value of the specific enthalpy corresponding to the extracted mass flow rate, but the difference to the specific hydrogen enthalpy h in the tank is decisive. It also becomes evident that in the single-phase region, where $h_{vent} = h$ and $h_{disch} = h$, the enthalpy streams for venting and discharge drop out and, in the case of discharge or dormancy simulations, the amount of hydrogen extracted from the tank only influences the hydrogen temperature by means of the term in the fourth row of Equation (5). The last row of the balance shows the heat flows from the solid tank material and the internal heat exchanger to the hydrogen.

Whereas the effect of the enthalpy streams and heat flows is also visible in the implicit form in Equation (2), the fourth row of Equation (5) results from reformulating the internal energy. The thermodynamic meaning of the term becomes evident when analyzing it for the case of an ideal gas.

With the ideal gas law

$$p \cdot v = R \cdot T, \tag{6}$$

$\left(\frac{\partial p}{\partial T} \right)_\varrho = \frac{R}{v}$ is valid and the fourth row of Equation (5) can be written as follows:

$$
\begin{aligned}
\frac{T}{\varrho} \cdot \left(\frac{\partial p}{\partial T} \right)_\varrho \cdot \left(\dot{M}_{fuel} - \dot{M}_{disch} - \dot{M}_{vent} \right) & \\
\overset{\text{ideal gas}}{=} \frac{T}{\varrho} \cdot \frac{R}{v} \cdot \left(\dot{M}_{fuel} - \dot{M}_{disch} - \dot{M}_{vent} \right) & \\
\overset{\text{ideal gas}}{=} p \cdot v \cdot \left(\dot{M}_{fuel} - \dot{M}_{disch} - \dot{M}_{vent} \right) .
\end{aligned}
\tag{7}
$$

The remaining term describes flow work due to the mass flows in and out of the tank. Since real fluid behavior of the hydrogen is considered in this paper, the original term can be interpreted as a modified net flow work including effects of the real fluid behavior. Thus, the change of the hydrogen temperature $\frac{dT}{dt}$ results from the specific enthalpy differences of the extracted and inserted mass flows compared to the tank, the flow work due to the mass flows, and the heat flows across the system boundaries.

Finally, a third differential equation is needed for the desired DAE system. Therefore, the right side of Fig. 5 shows the system of the solid tank shell. It consists of an aluminum liner and a carbon fiber layer wrapped around it. However, no distinction is made between both materials as they are assumed to be in perfect contact, allowing the use of one block temperature. As shown in Fig. 5, only two heat flows need to be considered to balance the solid: The heat flow $\dot{Q}_s$ from the solid to the hydrogen due to natural convection, also included in Equation (5), and the heat flow $\dot{Q}_{amb}$ from the ambiance to the solid. The latter results from the temperature difference between the solid material and the ambiance. In the case of CcH2 and sLH2, the tank is insulated by vacuum and a Multi-Layer Insulation (MLI) to keep the heat input low.

The implicit energy balance for the solid's internal energy U_s in Equation (8) can be derived and reformulated to the final explicit equation for the solid's temperature T_s in Equation (9):

$$\frac{dU_s}{dt} = \dot{Q}_{amb} - \dot{Q}_s \tag{8}$$

$$M_s c_s \cdot \frac{dT_s}{dt} = \dot{Q}_{amb} - \dot{Q}_s . \tag{9}$$

Thereby, the term $M_s c_s$ is used as an abbreviation for the sum of the products of the masses M and specific heat capacities c for the two solid materials aluminum (index: alu) and carbon fiber (index: cf):

$$M_s c_s = M_{alu} \cdot c_{alu}(T_s) + M_{cf} \cdot c_{cf}(T_s) . \tag{10}$$

With the three balance equations, Equation (1), Equation (5), and Equation (9), the three differential equations of the considered DAE system are derived. However, partial derivatives, such as $\left(\frac{\partial p}{\partial T} \right)_\varrho$, are only defined in the single-phase region. As the hydrogen energy balance Equation (5) includes two partial derivatives, $\left(\frac{\partial p}{\partial T} \right)_\varrho$ and $c_v = \left(\frac{\partial u}{\partial T} \right)_v$, it cannot be used to simulate processes in the two-phase region that are vital when considering, e.g., sLH2. Thus, an adaptation of the equations for two-phase operations is required.

2.3. Two-phase adaptation

In the two-phase region, the energy balance needs to be switched as the partial derivatives are not defined. Thereby, the property c_{v2P} is used. It is calculated in the two-phase region as follows from the vapor fraction x and the values at saturated liquid and vapor, c'_{v2P} respectively c''_{v2P}, which are provided by REFPROP [2]:

$$c_{v2P} = x \cdot c''_{v2P} + (1 - x) \cdot c'_{v2P} . \tag{11}$$

While the property c_{v2P} can be understood as a generic "specific isochoric two-phase heat capacity", its derivation and thermodynamic interpretation goes beyond and is further explained in Appendix A.3. As shown there, c_{v2P} is defined in a way that allows the formulation of the energy balance in the two-phase region similar to the formulation in the single-phase region, resulting in Equation (12):

$$
\begin{aligned}
M \cdot c_{v2P} \cdot \frac{dT}{dt} = & \dot{M}_{fuel} \cdot \left(h_{fuel} - h \right) \\
& - \dot{M}_{vent} \cdot \left(h_{vent} - h \right) \\
& - \dot{M}_{disch} \cdot \left(h_{disch} - h \right) \\
& + \frac{T}{\varrho} \cdot \left(\frac{dp_{sat}}{dT} \right) \cdot \left(\dot{M}_{fuel} - \dot{M}_{disch} - \dot{M}_{vent} \right) \\
& + \dot{Q}_s + \dot{Q}_{disch} .
\end{aligned}
\tag{12}
$$

Only the single-phase properties c_v and $\left(\frac{\partial p}{\partial T}\right)_\varrho$ are replaced by c_{v2P} and $\frac{dp_{sat}}{dT}$, respectively. The latter term describes the change of the saturation pressure along with the temperature.

2.4. Algebraic equations

Finally, the DAE system is completed by a set of algebraic equations. Hereby, the three operating modes need to be considered, as for each mode a different equation configuration is defined. However, in all three modes, the differential equations and the first four algebraic equations (Equation (13) to (16)) are identical:

$$\dot{Q}_s = \alpha_s \cdot A_i \cdot (T_s - T) \tag{13}$$

$$\dot{Q}_{amb} = k_{amb} \cdot A_o \cdot (T_{amb} - T_s) \tag{14}$$

$$\varrho = \frac{M}{V_{tank}} \tag{15}$$

$$h = h(T, \varrho) \, . \tag{16}$$

The first two algebraic equations describe the heat flows from the solid to the hydrogen $\dot{Q}_s$ (Equation (13)) and from the ambiance to the solid $\dot{Q}_{amb}$ (Equation (14)), as illustrated in Fig. 5. Thereby, $\dot{Q}_s$ is assumed to result from natural convection and is calculated from a heat transfer coefficient α_s, the inner tank area A_i, which is available for the heat transfer, and the temperature difference between the solid and the hydrogen. The heat transfer coefficient α_s is calculated according to the correlation by Kuehn and Goldstein [55] for heat transfer in horizontal cylindrical annuli. For $\dot{Q}_{amb}$, the outer tank area A_o, the temperature difference between the ambiance and the solid, and a heat transfer coefficient k_{amb} is used. k_{amb} results from convection and conduction and is highly dependent on the insulation used for the tank. In this paper, k_{amb} is defined in such a way that typical heat flow for the specific storage technology (CcH2, sLH2, and CH2) is reached. Further detail is given in Section 3 and in Table 1. The density ϱ of the hydrogen is calculated in Equation (15) and follows from the hydrogen mass and the tank volume V_{tank}. Finally, the specific enthalpy h of the hydrogen is calculated using REFPROP [2].

Similar to Hamacher et al. [1], the remaining three equations required to fully describe the system are defined specifically for each operating mode and are shown hereafter.

2.4.1. Standard operation mode

In the standard operation mode (equation configuration A), neither the minimum nor the maximum pressure needs to be hold, meaning that the internal heat exchanger is switched off and no hydrogen is vented. Thus, the remaining equations become trivial, as the heat stream resulting from the internal heat exchanger $\dot{Q}_{disch}$ and the venting mass flow $\dot{M}_{vent}$ are set to zero and the pressure is calculated using REFPROP [2]:

$$p = p(T, \varrho) \tag{17}$$

$$\dot{Q}_{disch} = 0 \tag{18}$$

$$\dot{M}_{vent} = 0 \, . \tag{19}$$

2.4.2. Minimum pressure mode

When the truck is at the minimum pressure mode (equation configuration B), the internal heat exchanger is switched on to keep the minimum pressure. The minimum pressure mode can only appear during the discharge operating scenario. It is assumed that it always delivers exactly the heat flow $\dot{Q}_{disch}$ required to keep the pressure. Further, no venting is required. Thus, two trivial equations result for the venting mass flow and the pressure:

$$p = p_{min} \tag{20}$$

$$\dot{M}_{vent} = 0 \, . \tag{21}$$

The final algebraic equation determines the required heat flow $\dot{Q}_{disch}$ from the internal heat exchanger to keep the minimum pressure. It is derived from the energy balance Equation (5), using the boundary condition that the pressure is constant for the special case of the minimum pressure operating mode. The derivation is further explained in Appendix A.4. For the single-phase region, Equation (22) follows:

$$\dot{Q}_{disch} = \dot{M}_{disch} \cdot \left[\frac{T}{\varrho} \cdot \left(\frac{\partial p}{\partial T}\right)_\varrho - \varrho \cdot c_v \cdot \left(\frac{\partial T}{\partial \varrho}\right)_p + h_{disch} - h \right] - \dot{Q}_s \, . \tag{22}$$

It is evident that the heat flow $\dot{Q}_s$ from the solid tank, and consequently, the heat flow $\dot{Q}_{amb}$ from the ambiance, reduces the heating demand. As a result, a higher heat leakage corresponds to a lower heat transfer requirement through the internal heat exchanger. However, due to the relatively small magnitude of the heat leak, its impact remains minor. On the other hand, the discharge mass flow $\dot{M}_{disch}$ has a significant influence since it is multiplied by all remaining terms within the brackets in Equation (22). Given that the first partial derivative within the brackets $\left(\frac{\partial p}{\partial T}\right)_\varrho$ is positive, the required heat flow rises with increasing temperature T and decreasing density ϱ. Since the second partial derivative $\left(\frac{\partial T}{\partial \varrho}\right)_p$ is always negative, the overall term $-\varrho \cdot c_v \cdot \left(\frac{\partial T}{\partial \varrho}\right)_p$ is positive again. In this context, a higher density would increase the heat requirement. Therefore, the net influence of density is not straightforward and depends on whether $\frac{T}{\varrho} \cdot \left(\frac{\partial p}{\partial T}\right)_\varrho$ or $\varrho \cdot c_v \cdot \left(\frac{\partial T}{\partial \varrho}\right)_p$ prevails. Since Equation (22) is only used for the single-phase region, where $h_{disch} = h$, the last term within the brackets always drops out.

In the two-phase region, the energy balance of the two-phase equation system Equation (12) is used as a basis for deriving the required heat flow, resulting in Equation (23):

$$\dot{Q}_{disch} = \dot{M}_{disch} \cdot \left[\frac{T}{\varrho} \cdot \frac{dp_{sat}}{dT} + h_{disch} - h \right] - \dot{Q}_s \, . \tag{23}$$

A more detailed derivation is provided in Appendix A.4 in Equations (A.53) and (A.54). Notably, the term $\varrho \cdot c_v \cdot \left(\frac{\partial T}{\partial \varrho}\right)_p$ does not have a counterpart in the two-phase case since in the two-phase region, the temperature must be constant when the pressure is constant. Furthermore, in the two-phase region, the term $h_{disch} - h$ influences the heat flow calculation. In the base case of this study, it is assumed that only liquid hydrogen is discharged in the two-phase region. Then, this term becomes negative, since the liquid phase is the less energetic phase ($h_{disch} = h' < h$). Consequently, the overall heat requirement is reduced by discharging liquid hydrogen. When, instead, only gaseous hydrogen is discharged, the term $h_{disch} - h$ would become positive and increase the heating requirement ($h_{disch} = h'' > h$).

2.4.3. Maximum pressure mode

In the maximum pressure mode, which only happens during the dormancy operating scenario, the venting pressure p_{vent} is reached. Therefore, hydrogen is withdrawn in order to keep the pressure. Again, two trivial equations are used for the pressure and the heat flow from the internal heat exchanger to the hydrogen:

$$p = p_{vent} \tag{24}$$

$$\dot{Q}_{disch} = 0 \, . \tag{25}$$

Similar to Equation (22) in the minimum pressure mode, Equation (26) is derived from the energy balance (Equation (5)) and defines the mass flow of hydrogen that needs to be vented in order to keep the pressure. A detailed derivation can be found in Appendix A.5:

$$\dot{M}_{vent} = \frac{\dot{Q}_s}{\frac{T}{\varrho} \cdot \left(\frac{\partial p}{\partial T}\right)_\varrho - \varrho \cdot c_v \cdot \left(\frac{\partial T}{\partial \varrho}\right)_p + h_{vent} - h} \, . \tag{26}$$

As expected, in this operation mode, the heat leak is disadvantageous since the mass flow rate that needs to be vented is higher when more heat $\dot{Q}_s$ is transferred from solid to the hydrogen. Furthermore, the same terms affecting the heat requirement in Equation (22) now influence the required venting mass flow rate. As such, a higher temperature will reduce the hydrogen loss. Once more, the influence of the density depends on which of the partial derivatives is predominant.

In the two-phase region, again the energy balance for the two-phase region (Equation (12)) is used as a basis for the derivation, resulting in (27):

$$\dot{M}_{\text{vent}} = \frac{\dot{Q}_s}{\frac{T}{\varrho} \cdot \frac{\mathrm{d}p_{\text{sat}}}{\mathrm{d}T} + h_{\text{vent}} - h} \ . \tag{27}$$

A more detailed derivation can be found in Appendix A.5 in Equations (A.59) and (A.60). The second term of the denominator in Equation (26) has no equivalent, thus the influence of the density is clear: A decreased density would result in a lower venting mass flow rate. However, Equation (27) is only theoretical since all hydrogen storage systems studied in this paper start venting above the critical pressure and, thus, in the single-phase region.

2.5. Simplified refueling model

In contrast to the discharge and dormancy operating scenarios, where only mass flows out of the tank with defined specific enthalpies are considered, the refueling scenario is characterized by a mass flow into the tank. While the refueling mass flow rate is a simulation parameter that needs to be set to a constant value, the thermodynamic state of the refueled hydrogen depends on the conditions in the refueling station's storage tank and the pressure to which the hydrogen is compressed during refueling. Thus, a refueling model is required. In literature [56–61], several studies and models on hydrogen refueling stations for refueling with LH2 or CH2 are provided. However, for simplification reasons, only a high-level approach is applied in this paper.

While CH2 must be refueled from gaseous hydrogen and sLH2 must be refueled from liquid hydrogen, CcH2 could be refueled from both [62]. Here, CcH$_2$ is always refueled with liquid hydrogen. In the simple refueling model deployed in this paper, a distinction is made whether the currently simulated tank is refueled with liquid or gaseous hydrogen. However, any effects of precooling the refueling pipes and instruments are neglected. It should be further noted that in none of the models any hydrogen is vented during refueling. Additionally, any ramp-up procedures during refueling, as suggested by [38] are not considered for the sake of simplicity.

2.5.1. Liquid hydrogen refueling

First, refueling with liquid hydrogen is considered. The refueling procedure is modeled in the following, simplified way, similar to Hamacher et al. [1]: A pump extracts saturated liquid from a stationary tank at a typical storage pressure of 3 bar [38]. Thereby, the hydrogen is compressed to the current pressure p of the truck tank, which is a variable of the equation system introduced earlier. It is assumed that the conditions in the stationary tank are constant and that the refueling pump can be characterized by an isentropic efficiency. Then, the change in temperature due to the compression and, thus, the specific enthalpy h_{fuel} of the refueled hydrogen, is calculated by considering isentropic compression with the defined isentropic efficiency.

2.5.2. Gaseous hydrogen refueling

Usually, gaseous hydrogen refueling stations use multiple compression steps within a cascade scheme to achieve the high storage pressures of the CH2 truck tanks [57]. Most refueling stations include cooling units after or in between the compression steps [56]. In order to not exceed a standardized maximal temperature of 85 °C, the hydrogen is thereby cooled down to -33°C to -40°C [57,63,64]. Here, for simplification reasons, it is assumed that the hydrogen is first compressed to the

Table 1
Parameters used for the CcH2, sLH2, and CH2 tank systems in all simulations.

Parameter	CcH2	sLH2	CH2
Hydrogen type	para	para	normal
Aluminum mass M_{alu} in kg	100	50	100
Carbon fiber mass M_{cf} in kg	150	0	300
Tank volume V_{tank} in m^3	0.5	0.5	0.5
Outer tank area A_o in m^2	4.1	4.1	4.1
Inner tank area A_i in m^2	4.0	4.0	4.0
Heat transfer coefficient k_{amb} in W/(m^2 K)	0.025	0.005	50
Ambient temperature T_{amb} in K	298.15	298.15	298.15
Fill pressure p_{fill} in bar	400	16	700
Venting pressure p_{vent} in bar	450	20	/
Minimum pressure p_{min} in bar	15	6	15
Ideal stop density ϱ_{stop} in g/l	5.8	2.4	/

current tank pressure. Then, it is cooled down to -33 °C before it is fed to the tank. Thus, the condition of the hydrogen in the stationary tank is not relevant for this simplified model, as the thermodynamic state of the refueled hydrogen only depends on the tank pressure p.

3. Results

To demonstrate the capabilities of the derived model and to compare the three hydrogen storage technologies considered in this paper, CcH2, sLH2, and CH2, several simulations are performed in this section. First, a typical drive cycle in heavy-duty truck applications is simulated for all storage types. Afterward, a closer look at CcH2 and sLH2 operating strategies is provided by showing comparisons concerning the heat requirements during discharge, the dormancy times, and finally, optimal stopping criteria for the discharge mode.

However, several parameters must first be set to fully describe the three considered tank systems. Table 1 lists the parameters used for all simulations with the CcH2, sLH2, and CH2 tanks. The first row defines the hydrogen type used for all property data calls with REFPROP [2]. For CH2, normal hydrogen is used, as the tank is at ambient temperatures and, thus, equilibrium composition is assumed.

Instead, for CcH2 and sLH2, para hydrogen is used. This assumption is justified since for both technologies, only refueling with liquid hydrogen is considered in this paper. As in liquid hydrogen, almost only para hydrogen exists, and the conversion from para hydrogen to ortho hydrogen is relatively slow, assuming CcH2 and sLH2 to be entirely composed of para hydrogen is reasonable [37,49]. According to Petitpas et al. [49], the conversion significantly affects the thermodynamics after 10 to 15 days at temperatures around 70 K to 80 K, which is out of scope for a typical heavy-duty truck operation schedule. Only when considering unscheduled and long standing times, e.g., for maintenance, the para-ortho conversion would become relevant. However, as the conversion would cool down the tank, it would counteract heat entry from the environment and extend loss-free dormancy times [37,47,49]. Thus, not considering the conversion for dormancy studies is rather conservative.

Further parameters shown in Table 1 concern the geometry and composition of the tanks. Thereby, typical values are chosen. Same as in Hamacher et al. [1], each tank is supposed to have a volume of 0.5 m^3 and an internal surface area of 4 m^2. The outer surface area of the solid tank is assumed to be slightly higher. In a CcH2 tank, approximately 40 kg of hydrogen could be stored. That way, two tanks could deliver a driving range of 1000 km in a typical heavy-duty truck application [26].

Considering the tank materials, the different tank types used for storing the hydrogen must first be defined to determine typical component masses. As the solid tank material is in direct contact with the hydrogen, it significantly influences the thermodynamic state of the hydrogen. The CcH2 tank is typically a type III tank. Therefore, as in Hamacher et al. [1], an aluminum mass of 100 kg and a carbon fiber mass of 150 kg is used. To withstand high pressures of up to 700 bar in CH2 tanks, type

III or type IV tanks are required [6]. For better comparability, a type III tank is chosen for CH2. Analogously to the CcH2 tank, an aluminum mass of 100 kg is assumed. However, to acknowledge the far higher pressure range, a larger carbon fiber layer and, thus, a higher carbon fiber mass of 300 kg is assumed, which corresponds to roughly scaling up literature values [47]. As an sLH2 tank does not need to withstand high pressure, insulated low-pressure tanks without carbon fiber wrappings are used. For this study, an aluminum mass of 50 kg is assumed, which lies within values suggested by Ahluwalia et al. [35].

For simplification reasons, the insulation of the tanks is not modeled in this paper. Instead, the heat entry from the environment is calculated with Equation (14). Therefore, each tank's insulation characteristics are represented by the heat transfer coefficient k_{amb}. As this value is hard to determine and highly depends on the insulation used, the values shown in Table 1 are only estimates that are assumed constant and independent of the tank and ambient conditions. As CH2 is stored at ambient temperature and, thus, does not need insulation, a typical value of $k_{amb} = 50\ \text{W/(m}^2\text{K)}$ for natural convection, considering a horizontal cylinder within the air, is used. As the tanks are not directly exposed to the ambient air stream during driving, forced convection is not further considered.

In contrast, the heat transfer coefficient of CcH2 and sLH2 are defined so that a typical heat leak of 5 W for sLH2 and 25 W for CcH2 is approximately reached at cryogenic tank conditions. The resulting values correspond to standard heat leak specifications of an MLI, which typically range within a few W/m² [35,65]. Since the insulation requirement of sLH2 is higher compared to CcH2, the heat leak of sLH2 is also chosen to be smaller. Furthermore, for all simulations a constant ambient temperature of 298.15 K is defined.

Finally, some boundary conditions are set for the different operating scenarios and modes. The fill pressure p_{fill} defines the end of every refueling simulation. For CcH2, a fill pressure of 400 bar [26], and for sLH2, a fill pressure of 16 bar [22,66] is used. In the case of CH2, a high-pressure tank with a fill pressure of 700 bar [32] is considered.

Additionally, venting pressures p_{vent} are defined for all tank types. These correspond to a maximal allowed system pressure. When exceeding the venting pressure, hydrogen must be vented from the tank to hold the pressure. As venting is not only non-economically but also has potential environmental risks [67], the vented mass should be kept as small as possible. For CcH2, a typical value for type III tanks is chosen with 450 bar [27]. This value also corresponds to Moreno-Blanco et al. [47], who state that the vent valve typically opens 50 bar above the design pressure. The value chosen for sLH2 is also based on literature [68]. In the case of the CH2 tank, the venting pressure is irrelevant for this study, as CH2 is stored at ambient temperature. Thus, no significant pressure increase is expected when considering dormancy.

Furthermore, a minimum pressure p_{min} is defined for all tanks, which mainly depends on the pressure level required for the FC. For CcH2 and CH2, a minimum pressure level of 15 bar to fuel the FC is set [26]. When considering sLH2, a lower minimum pressure of 6 bar is used [68]. This means that the considered sLH2 truck requires an FC that is able to operate at lower pressures. Otherwise pumps onboard the truck would be required [35]. When considering CcH2 and sLH2, the minimum pressure p_{min} defines the point at which the internal heat exchanger needs to be switched on to hold the pressure. In CH2, however, reaching the minimum pressure is a stop condition for driving. In CcH2 and sLH2 tanks, instead, an ideal stop density ϱ_{stop} is defined as stopping criteria. Its derivation is shown later on in Section 3.4.

Table 2 further summarizes the full tank starting conditions of each tank system. These values are used as starting conditions for all drive cycle simulations and are considered to represent a full tank. They are selected in such a way that in a drive cycle, the end of refueling equals the starting conditions of a discharge. Additionally, for all discharge simulations, a constant discharge mass flow of $\dot{M}_{disch} = 1\ \text{g/s}$ and for all refueling simulations, a constant refueling mass flow of $\dot{M}_{fuel} = 70\ \text{g/s}$ is used.

Table 2
Full tank starting condition.

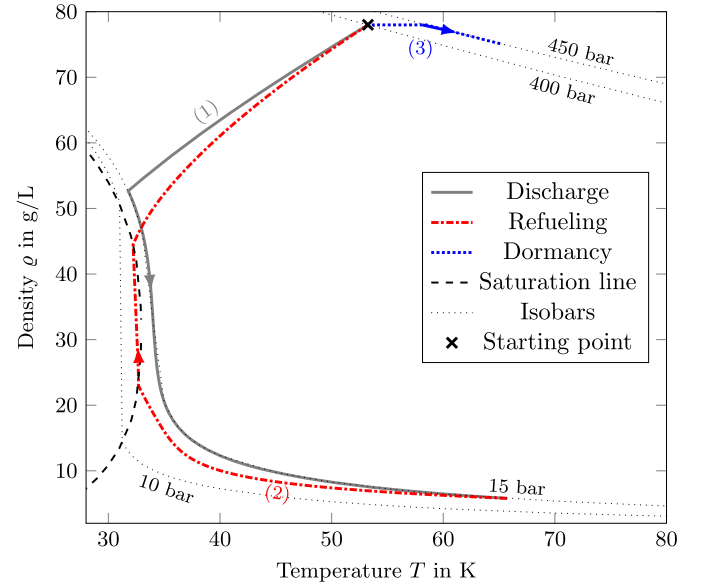| Parameter	CcH2	sLH2	CH2
Pressure p in bar	400	16	700
Temperature T in K	53.25	28.20	331.6
Density ϱ in g/l	78.00	62.07	36.36

Fig. 6. Drive cycle simulation consisting of discharge until the tank is almost empty (1), refueling up to the fill pressure (2), and dormancy for 60 h (3) for CcH2. (For interpretation of the colors in the figure(s), the reader is referred to the web version of this article.)

3.1. Drive cycle simulation

The previously derived generalized model can simulate and, thus, compare hydrogen tanks of the three technologies: CcH2, sLH2, and CH2. Therefore, Fig. 6, Fig. 7, and Fig. 8 visualize a typical drive cycle simulation for all three options. In each simulation, the starting point was defined as a full tank at the conditions shown in Table 2. First, a discharge scenario with a constant discharge mass flow of $\dot{M}_{disch} = 1\ \text{g/s}$ out of the tank is simulated until a stop criterium is reached. In the case of CcH2 and sLH2, it is the optimal stop density ϱ_{stop}; in the case of CH2 it is the minimum operating pressure from Table 1. Even though the tank is not physically empty when this condition is reached, and at least CcH2 and sLH2 could theoretically be discharged to lower densities, driving further is not recommended. This will be explained in more detail in Section 3.4.

The time period required for the total discharge of the tank thereby depends on the hydrogen storage type or, more specifically, on the usable density that will be further discussed in Section 3.4. Right after the discharge, a refueling scenario is simulated. Here, all tanks are refilled with a constant refueling mass flow of $\dot{M}_{fuel} = 70\ \text{g/s}$ with the method described in Section 2.5 until the fill pressure of each tank is reached. Finally, 60 h of dormancy, which corresponds to 2.5 days, are simulated, starting from full tank conditions. This starting condition was chosen since the risk of venting is highest when the tank of the parked truck is full. It should be noted that all results generated in this section highly depend on the chosen design parameters.

Fig. 6, Fig. 7, and Fig. 8 show the process curves of the hydrogen in a temperature-density diagram. In addition, the saturation lines and relevant isobars are plotted. As para hydrogen is used to simulate CcH2 and sLH2, these curves are also calculated from para hydrogen data, whereas normal hydrogen is used for CH2. When comparing the plots shown in Fig. 6, Fig. 7, and Fig. 8 with the temperature-density diagram
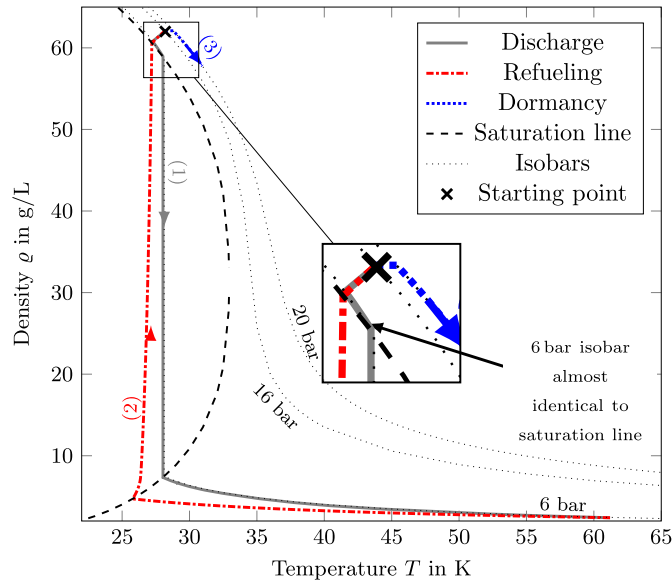
Fig. 7. Drive cycle simulation consisting of discharge until the tank is almost empty (1), refueling up to the fill pressure (2), and dormancy for 60 h (3) for sLH2.

Fig. 8. Drive cycle simulation consisting of discharge until the tank is almost empty (1), refueling up to the fill pressure (2), and dormancy for 60 h (3) for CH2.

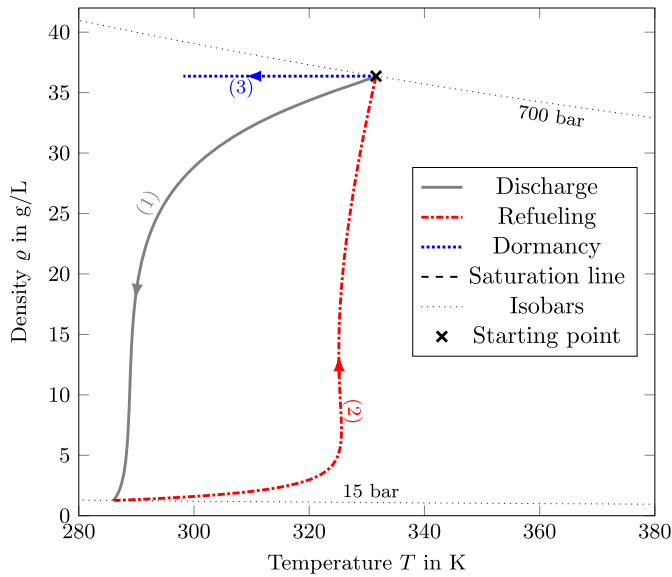in Fig. 1, it should be noted that the CH2 curve in Fig. 8 is located on the right side of Fig. 1, far away from the two-phase region, the sLH2 curve in Fig. 7 is located on the left side of Fig. 1, within the two-phase region, and the CcH2 curve in Fig. 6 is located in between, close to the two-phase region.

All simulations start at the marked starting points on the 400 bar, 16 bar, and 700 bar isobar, respectively. Then, in all cases, the temperature T, the density ϱ, and the pressure p of the hydrogen drop at the beginning of the discharge. This effect results from the flow work term corresponding to line four of Equation (5), which reduces the internal energy of the remaining hydrogen within the tank. The first three lines of Equation (5) do not affect this part of the discharge process since all tanks are in the single-phase region leading to $h_{\mathrm{disch}} = h$, and only the discharging mass flow $\dot{M}_{\mathrm{disch}}$ is unequal zero. Furthermore, since the tanks (at least for CcH2 and sLH2) are well insulated, the heat

transfer from the environment is very small. Consequently, the tank is near-adiabatic. Thus, near-isentropic expansion takes place within this first part of the discharge process. As a result, the decrease in internal energy leads to a decrease in temperature.

When looking at the discharge scenario of CH2 in Fig. 8, it can be noted that the slope of the curve rises and becomes very large when the temperature drops below 300 K, which equals roughly the defined constant ambient temperature of 298.15 K. However, shortly before the tank is empty, the slope decreases again. Considering Equation (5), here, the equation is simplified to

$$M \cdot c_v \cdot \frac{\mathrm{d}T}{\mathrm{d}t} = -\dot{M}_{\mathrm{disch}} \cdot \frac{T}{\varrho} \cdot \left(\frac{\partial p}{\partial T} \right)_\varrho + \dot{Q}_{\mathrm{s}}, \tag{28}$$

since no hydrogen is fueled or vented during the discharge scenario, the hydrogen is in single-phase state all the time, and no heat is added to the CH2 tank through an internal heat exchanger. While the density drops linearly over time, the change in the temperature is defined by the energy balance. At the beginning of the simulation, the temperature drops fast, corresponding to a small slope in the temperature-density diagram. Thereby, the heat flow $\dot{Q}_{\mathrm{s}}$ is negative, meaning that the hydrogen transfers heat over the tank's solids to the environment because the ambient temperature of 298.15 K is lower than the tank temperature. In contrast to the CcH2 and sLH2 tanks, the CH2 tank is not well insulated. Consequently, the influence of the heat flow to the ambiance is more relevant. Thus, in this range, both terms from Equation (28), the flow work term $-\dot{M}_{\mathrm{disch}} \cdot \frac{T}{\varrho} \cdot \left(\frac{\partial p}{\partial T} \right)_\varrho$ and the heat flow $\dot{Q}_s$, have the same effect: reducing the hydrogen temperature.

Since the ambient temperature is defined as 298.15 K in the simulation, the orientation of the heat flow changes at this point and the heat flow $\dot{Q}_{\mathrm{s}}$ becomes positive. This explains the first change of the slope in Fig. 8. Here, both effects contradict each other: the flow work term leads to a reduction of the hydrogen temperature, which is weakened by the heat leak from the ambiance. Thus, in this range, the temperature decrease becomes very small, resulting in a steep slope in Fig. 8.

However, to explain the final slope change at the end of the discharge scenario, a closer look at the flow work term is required. Whereas the density ϱ still drops linearly with time, the temperature decreases very slowly due to the opposite effects of flow work and heat leak. The faster reduction of the density than the temperature results in a near-exponential increase of the term $\frac{T}{\varrho}$ in this region. Furthermore, the slope of the isobars becomes very small at low densities (see Fig. 1), which results in an increase of $\left(\frac{\partial p}{\partial T} \right)_\varrho$. Thus, the flow work term is dominating in this area and the temperature finally drops faster again.

When considering CcH2 and sLH2 in Fig. 6 and Fig. 7, the discharge process is split into two parts. In the first part, temperature, pressure, and density drop analogously to CH2. However, here, the heat flow from the ambiance plays a minor role as both tanks are well insulated. When the minimum system pressure p_{min} is reached, the internal heat exchanger is switched on. As a result, in the second part, the tank is heated in order to keep that pressure. For CcH2, this means that the curve follows the 15 bar isobar. Furthermore, the course of the CcH2 is nearly identical to the results of Hamacher et al. [1], which shows that distinguishing between the temperature of the solids and the hydrogen only has a minor influence.

When looking at sLH2, the curve is further influenced by the phase state of hydrogen. Here, the hydrogen is completely liquid in the first part of the discharge without heating, which is enlarged in the detail excerpt of Fig. 7. Furthermore, the period without heating is significantly shorter compared to CcH2. Close before the saturation line is reached, the hydrogen reaches the minimum system pressure of 6 bar and the internal heat exchanger is switched on. Thus, the curve follows the isobar, which is very close to the saturation line in this area. At some point, the saturation line is crossed, meaning that the hydrogen now enters the two-phase region at a density of approximately 58.2 g/L. Within the two-phase region, the temperature is constant with constant pressure.

Finally, the curve crosses the saturation line again when no liquid is left at a density of approximately 7.6 g/L. Then, only gaseous hydrogen is left. However, it is assumed that the discharge system is also capable of discharging gaseous hydrogen and that the process can continue until the desired stop density is reached.

After the discharge, a refueling simulation (2) is visualized for all cases in Fig. 6, Fig. 7, and Fig. 8, starting with the final values of the discharge simulation. The course of CH2 in Fig. 8 is almost directly opposed to the discharging scenario. This results from the same effects as during discharge, however this time the relevant mass flow rate $\dot{M}_{\text{fuel}}$ flows into the tank. At the end of the refueling, the starting point of the previous discharge simulation is reached again.

In the CcH2 and sLH2 cases in Fig. 6 and Fig. 7, the refueling curves also end at the starting point of the discharge scenario. However, in both cases, the two-phase region is crossed during the refueling process. At the beginning of the refueling, the pressure and the temperature of the hydrogen in the tank drop. The density, instead, rises linearly with time since the refueling mass flow rate is constant. The drop in temperature and pressure can be explained by the cooling effect of the refueled hydrogen, which comes from a liquid hydrogen station and is stored at colder temperatures than the hydrogen in the tank. In Equation (5), the cooling effect corresponds to the term $\dot{M}_{\text{fuel}} \cdot (h_{\text{fuel}} - h)$. However, after a certain amount of time, the pressure and temperature in the tank rise when the pressurization effect from pushing in more hydrogen into the tank dominates over the cooling effect. In Equation (5), the pressurization effect corresponds to the term $\frac{T}{\varrho} \cdot \left(\frac{\partial p}{\partial T}\right)_{\varrho} \cdot \dot{M}_{\text{fuel}}$.

Considering the CcH2 curve, a similar behavior, as stated in Hamacher et al. [1], is observed. Small deviations result from the separate consideration of the solid temperature and the hydrogen temperature, as the solid's thermal mass reacts delayed to changes in the hydrogen temperature and, thus, dampens the course. First, the hydrogen is supercritical. As the temperature and pressure drop, the hydrogen becomes gaseous before entering the two-phase region. Within the two-phase region, the slope of the curve appears almost vertical, but temperature and pressure further decrease. After the two-phase region, the hydrogen in the tank is fully liquid and the pressurization starts. Hence, temperature and pressure rise and the hydrogen becomes supercritical. As the hydrogen mass becomes larger during refueling, the influence of the solid tank material becomes less relevant and the final state is almost equivalent to the results from Hamacher et al. [1]. This shows that a separate consideration of hydrogen and solid temperature is slightly relevant only for short-time-scale operations like refueling. However, in long-time-scale operations like discharge or dormancy, it becomes almost irrelevant. It should be further noted that the discussed behavior is only valid for refueling with liquid hydrogen. CcH2 tanks can also be refueled with gaseous hydrogen. In that case, no cooling effect will be obtained.

The sLH2 curve shows a very similar behavior as CcH2. First, in the single-phase gas region, temperature and pressure decrease since the cooling effect dominates the pressurization. However, when entering the two-phase region, the pressurization effect exceeds the cooling effect due to a sudden increase of $\frac{\mathrm{d}p_{\text{sat}}}{\mathrm{d}T}$ compared to $\left(\frac{\partial p}{\partial T}\right)_{\varrho}$ at the phase boundary. Thus, in the two-phase region the temperature and pressure increase slightly. Right after the phase boundary, the temperature increases faster than during the rest of the two-phase operation. Again, this can be explained by the delayed reaction of the thermal mass of the solid tank. Before reaching the two-phase area, the hydrogen temperature was decreasing fast. The solid temperature was also decreasing, however much slower than the hydrogen. Now, at the phase boundary, the change of the hydrogen temperature is slower as most of the cooling effect is used to condensate hydrogen. Since at this point, the solid is significantly warmer than the hydrogen, it now additionally heats up the hydrogen until the temperatures assimilate. Thus, in this small period of time, the heat from the solid to the hydrogen dominates the pressurization and the cooling effect of the refueled hydrogen.
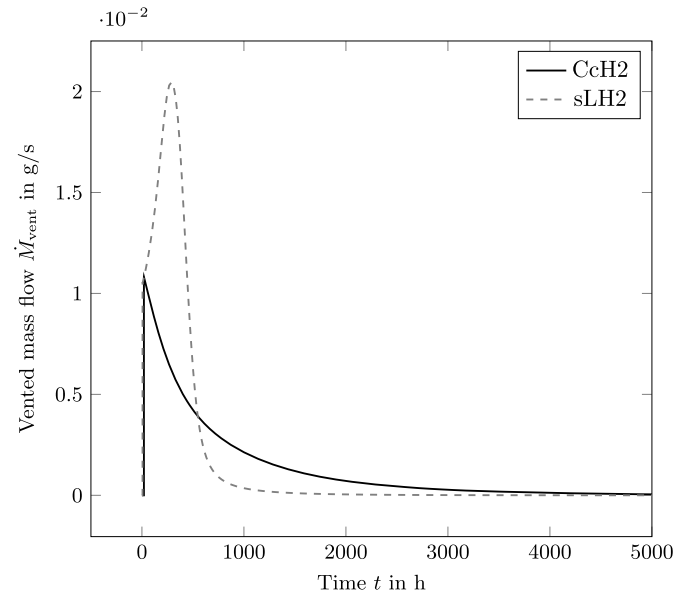

Fig. 9. Vented mass flow rate over dormancy time for CcH2 and sLH2.

Finally, the simulation of 60 h of dormancy (3) starting from the final conditions after refueling, as visualized in Fig. 6, and Fig. 7, Fig. 8, needs to be discussed. In the case of CH2, the temperature after refueling is above the ambient temperature due to the pressurization of refueling. Thus, the temperature in the tank, and therefore also the pressure, slowly decreases during the dormancy. When the tank temperature has reached the ambient temperature, no more changes are observed. As a result, venting during dormancy is not expected for CH2 tanks. In the CcH2 and sLH2 tanks, instead, the temperature and pressure first rise due to the heat leak from the ambiance until the maximum system pressure p_{vent} is reached. Then, hydrogen is vented from the tank to keep that pressure. When avoiding dormancy with a full tank, e.g., by refueling before a drive instead of after a drive, venting can also be avoided for CcH2 and sLH2. However, even after a relatively long dormancy time of 60 h, both tanks are still at low temperatures and high densities. The dormancy behavior of both tanks is further discussed hereafter.

3.2. Comparison of the dormancy behavior of CcH2 and sLH2

To further study the dormancy behavior of CcH2 and sLH2, another dormancy simulation with a larger time scale was conducted. Fig. 9 shows the vented mass flow rate over dormancy time for CcH2 and sLH2.

At the beginning of the simulation, starting from full tank conditions, the vented mass flow is zero in both tanks. Due to the long time scale in Fig. 9, the vent-free time is hardly visible. However, the simulations have shown that the venting starts earlier for sLH2 after approximately 6 h, while the CcH2 tank needs to start venting roughly three times later after 19.5 h for the considered design and simulation parameters. Thus, in typical operation, where trucks are driven daily, no venting is to be expected.

At the beginning of the venting, the vented mass flow rates of both storage systems rise immediately to a value of approximately $1 \cdot 10^{-2}$ g/s. While the vented mass flow of CcH2 monotonously drops afterward and approaches zero after approximately 5000 h, the vented mass flow rate of sLH2 first increases further to $2 \cdot 10^{-2}$ g/s and then decreases again and approaches zero faster than CcH2 after approximately 2000 h. This behavior relates to the course of the respective isobars of the venting pressure p_{vent}. For the relatively high venting pressure of 450 bar for CcH2, the slope of the isobar constantly decreases in the temperature-density diagram (Fig. 1). Thus, with time and rising tank temperature, the decrease of the density ϱ in the tank is low and less
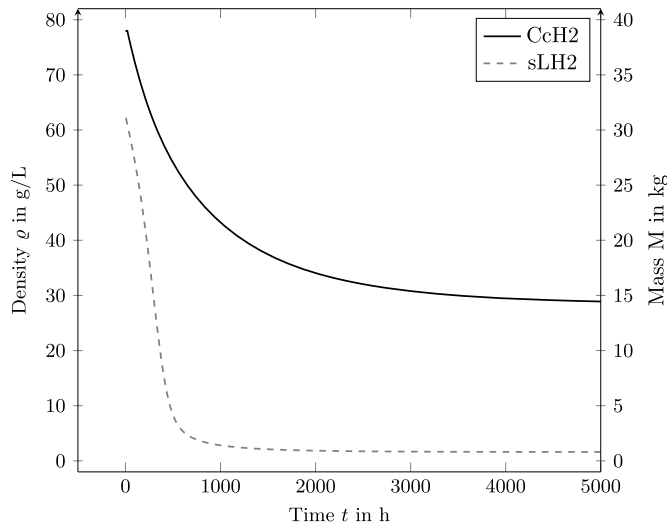
Fig. 10. Density and mass of the hydrogen left in one single tank during dormancy for CcH2 and sLH2.

Fig. 11. Heat flow required for CcH2 and sLH2 tanks to not fall below the minimum system pressure during discharge with 1 g/s.

mass must be vented from the tank to keep the pressure. Additionally, the temperature rises slower with time since the temperature difference between the solid tank and the ambiance and, thus, the driving force of the heat transfer (Equation (14)) becomes smaller with rising tank temperature. However, in this paper, the heat transfer between the solid and the ambient is modeled in a simplified way. As such, the solid is considered to have one uniform block temperature. Thus, heat conduction effects are neglected. Additionally, the heat transfer through the MLI is not modeled in detail. Instead, for the sake of simplicity, it is considered by a constant heat transfer coefficient k_{amb}. In real application, a non-linear correlation between heat loss and temperature is expected, as the heat transfer coefficient and the heat conductivity of the materials also depend on temperature.

The isobar of the relatively small venting pressure of 20 bar for sLH2 behaves differently, as can be seen in Fig. 7. The slope of the isobar in the temperature-density diagram first increases and becomes steep in a temperature range between 30 K to 40 K. This means that the decrease of the density ϱ is high and larger amounts of hydrogen need to be vented from the tank to keep the pressure, resulting in the increase of the venting mass flow rate in Fig. 9. Then, at low densities, the isobar's slope decreases much faster than the slope of the 450 bar isobar and becomes almost horizontal. Thus, in this range, the amount of vented hydrogen also becomes small and approaches zero quickly. In both tanks, the vented mass flow rate finally becomes zero when the tank temperature reaches the ambient temperature.

Besides the vented mass flow rate, the mass of hydrogen left in the tank after venting is also relevant for operation. As the tank volumes are equal in all simulations ($V_{tank} = 0.5\,\text{m}^3$), the density is also a measure of the hydrogen mass in the tank. Thus, Fig. 10 shows the mass M alongside the density ϱ of the remaining hydrogen over time for a dormancy simulation for CcH2 and sLH2. Thereby, the mass corresponds to one single tank. Typically, more than one tank is used in truck applications, thus the overall stored hydrogen mass could be higher.

Due to venting, the mass and density are reduced in both curves. Fig. 9 shows that the vented mass flow rate approaches zero with time when the tank temperature approaches to the ambient temperature. This means that the density and mass in the tank in Fig. 10 will approach a constant value. For an ambient temperature of 298.15 K, the density of the CcH2 tank will not drop below 36.4% of the fill density. For sLH2, the minimal remaining density is significantly lower with approximately 1.3% of the fill density. Again, these values highly depend on the considered design and simulation parameters.
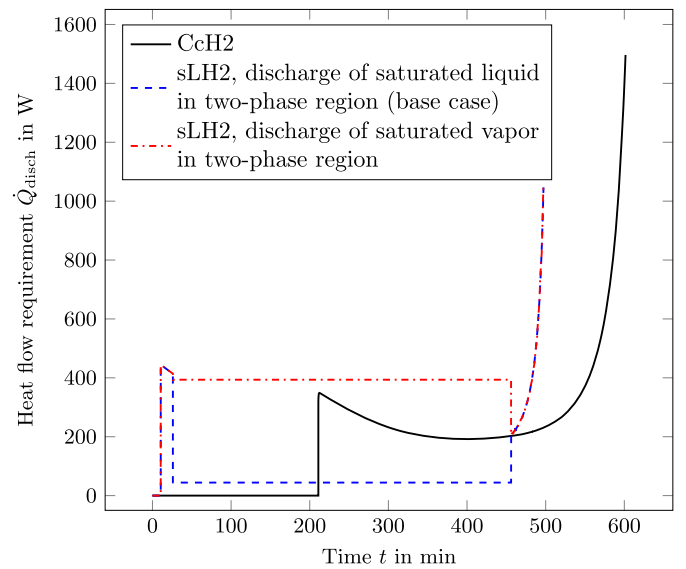
3.3. Heat requirement during discharge

When considering discharge, the CcH2 and sLH2 tanks require additional heat from an internal heat exchanger to keep a minimum system pressure, as discussed in Section 3.1. Here, a closer look at the heat requirement is provided. Fig. 11 shows the required heat flow rate $\dot{Q}_{disch}$ to keep the minimum system pressures versus time for a discharge simulation starting from the conditions set in Table 2. However, it should be noted that the values shown are highly dependent on the minimum system pressure, defined in Table 1, and the mass flow rate of the discharge. For sLH2, the base case of discharging saturated liquid in the two-phase region is further compared to discharging saturated vapor in the two-phase region.

The curve for CcH2 looks very similar to the results from Hamacher et al. [1], thus, the separate consideration of solid and hydrogen temperature has a minor influence. When the minimum pressure is reached after approximately 200 min, the internal heat exchanger is switched on. Consequently, the heat flow requirement jumps to a value of roughly 400 W. Then, the heat flow first decreases before steeply increasing towards the end. This behavior follows from the slope of the isobar of the minimum pressure shown in Fig. 6. When the isobar gets steeper, the heat requirement becomes smaller because only a small change in temperature is required to keep the pressure. Towards the end of the discharge scenario, when the density is small, the isobar becomes flatter. There, a large change in temperature is needed to keep the pressure, thus a large amount of heat flow and consequently a fast-rising temperature of the hydrogen is required. The end of the curves are defined by the end of the simulation, when the minimal density is reached, which will be further discussed in Section 3.4

When the curve of the heat flow requirement for sLH2 with discharge of saturated liquid hydrogen in the two-phase region (base case) is considered, it can be recognized that the internal heat exchanger is switched on much earlier. Thus, the immediate jump of the heat flow happens earlier after only a few minutes. However, after the initial increase of the heat flow, the required heat flow suddenly drops again only a few minutes later. This happens when the hydrogen in the tank enters the two-phase region. Here, the course of the isobar becomes vertical, meaning that no change in temperature is required, but only the evaporation heat for the phase change of hydrogen needs to be added to the tank by the internal heat exchanger. As a result, the required heat flow becomes constant at a relatively low value within the two-phase region. As soon as the saturation line is crossed again and only gaseous
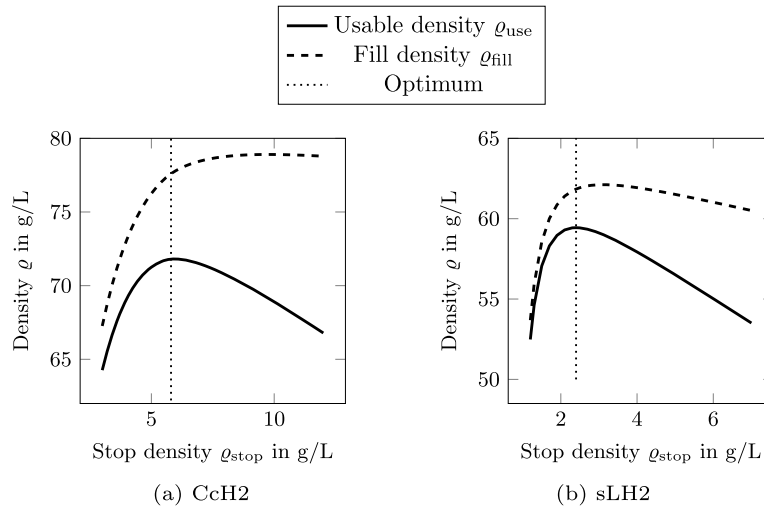
Fig. 12. Fill density and usable density depending on the stop density for CcH2 and sLH2.

hydrogen is left in the tank, the heat flow requirement jumps up again immediately. Afterward, it rises with a similar slope as the CcH2 curve because the minimum system pressure isobar becomes very flat in this range.

The course of the heat requirement of sLH2, when saturated vapor is discharged in the two-phase region, is equal to the base case for both single-phase periods. In the two-phase region, however, the heat requirement is much higher since the higher energetic phase is withdrawn from the tank and, thus, a higher heat flow is required to keep the pressure.

However, discharging liquid hydrogen in the base case also means that outside of the tank the hydrogen does not only need to be heated up for feeding it into the FC, but it also needs to be evaporated first, resulting in additional heat requirement in an outer heat exchanger. When, instead, vapor is discharged in the two-phase region, this additional heat requirement is shifted to the internal heat exchanger while the outer heat exchanger requires less heat flow.

Overall, the heat flow requirement is lower for sLH2, meaning the internal heat exchanger can be designed smaller.

3.4. Optimization of ideal stop density

Similar to the implicit tank model introduced by Hamacher et al. [1], the explicit model shown here also allows for conducting operation strategy optimizations. As shown earlier, toward the end of the CcH2 and sLH2 discharge procedures, the heat that must be put into the tank to hold the pressure increases tremendously. As a result, the temperature in the tank rises. However, for efficient refueling, a cold tank is advantageous. As seen before (Section 3.1), the CcH2 and sLH2 tanks are cooled down during refueling. When the tank is warmer at the beginning of the refueling, the overall temperature after refueling will also be warmer, which comes with lower densities at the same pressure. Thus, it is not recommended to discharge the tank until it is completely empty but to stop earlier to achieve the best usable density ϱ_{use}. The usable density is calculated from the fill density ϱ_{fill} and the stop density ϱ_{stop} by the following equation:

$$\varrho_{use} = \varrho_{fill} - \varrho_{stop}. \tag{29}$$

In Hamacher et al. [1], the usable density ϱ_{use} was already optimized for CcH2. In Fig. 12, the optimal stop densities of CcH2 and sLH2 are calculated and compared. The courses of the usable and the fill density are shown for a typical range of stop densities each. It can be seen that the usable density has an optimum at a stop density of 5.8 g/L for CcH2 and at a stop density of 2.4 g/L for sLH2. For CH2, no optimization is

required as no heat is actively added to the tank. Here, the stop density ϱ_{stop} equals the density left in the tank when the minimum pressure is reached. In the simulations made in Section 3.1, this corresponds to 1.26 g/L. However, it should be noted that these values highly depend on the geometrical and material parameters listed in Table 1. Qualitatively comparing the resulting usable densities, and thus, the driving ranges gives an approximately 70% higher driving range of sLH2 and an even 105% higher driving range of CcH2 compared to CH2.

Slight deviations in the CcH2 curve on the left side of Fig. 12 from the findings of Hamacher et al. [1] result from separately balancing the solid temperature and the hydrogen temperature. As discussed before in Section 3.1, the influence of this adaptation is slightly visible during short-time procedures as refueling.

Fig. 12 also shows that at the beginning, all curves rise with increasing stop density. This can be explained with the effect explained earlier at the beginning of this section. To reach these low stop densities, a lot of heat needs to be put into the tank which results in higher temperatures. This is a disadvantage for refueling as the fill density will be smaller.

However, looking at CcH2, the slope of the fill density curve becomes smaller and almost flattens. At these higher stop densities, less heat was added to the tank during discharge, meaning the tank is colder at the beginning of the refueling. When considering the course of the minimum system pressure isobar and, thus, the hydrogen state during discharge in Fig. 6, it can be seen that in this region, the isobar becomes steeper. Thus, stopping at even higher densities has little effect on the temperature. Consequently, there is no further advantage for the fill density and the usable density drops again.

When looking at the course of the usable and fill densities of sLH2, a similar behavior is visible. However, shortly after the optimum of the usable density, the fill density also drops. By closer consideration of the CcH2 fill density, the same behavior could be noticed. The reason for this finding is that the refueled hydrogen is always colder than the hydrogen in the tank. Thus, the overall temperature will be smallest when the hydrogen in the tank is not too warm but also when a lot of cold hydrogen is refueled. As a result, not just the usable density but also the fill density has an optimum. This effect is higher for sLH2 since, during most of the discharge process, the hydrogen is within the two-phase region, meaning that the temperature is constant at constant pressure. Thus, within this region, stopping earlier has no advantage regarding the tank temperature.

Comparing the curves of fill density and usable density for CcH2 and sLH2, it can be noted that ϱ_{fill} and ϱ_{use} differ less for sLH2 since the optimal stop density is lower compared to CcH2. However, ϱ_{fill} and ϱ_{use} are both smaller for sLH2 than for CcH2. Furthermore, stopping

to refuel before the optimal stop density is reached has only a small effect on the fill density of CcH2. This means, that if the truck stops earlier, the possible range was not fully exploited during this discharge. However, at the next discharge almost the full range is available again. For sLH2 instead, stopping for refueling too early will result in slightly less hydrogen being refueled and thus a shorter range.

4. Conclusion

In this paper, an explicit thermodynamic DAE system has been introduced that is able to describe physical hydrogen storage tanks for truck applications in all operating scenarios and operation modes. The model is a further development and generalization of the CcH2 tank model by Hamacher et al. [1]. Adaptations were made, including the separate consideration of the energy balances of the solid tank materials and the hydrogen. Additionally, the model was formulated in an explicit way, using the REFPROP [2] property c_{v2P}, which can be used analogously to a specific isochoric heat capacity in the two-phase region, for the energy balance during two-phase operation. This model formulation then allows the simulation of all possible operations of a heavy-duty truck tank within the gaseous, liquid, and two-phase regions. Between different operating conditions and the two-phase and single-phase regions, minor changes to the equation system are made automatically by a smart decision logic. Furthermore, the explicit model formulation allows for a deeper understanding of the processes within the tank. As an example, it shows that the hydrogen temperature drops during discharge because of a modified flow work, which is conducted by removing hydrogen from the tank, and a near-isentropic change of state.

The resulting model was then used to compare typical drive cycles of three physical hydrogen storage technologies: the current state-of-art CH2 and the currently developed CcH2 and sLH2 technologies. In comparison to the CcH2 tank model by Hamacher et al. [1], it has been shown that separating the solid energy balance from the hydrogen energy balance has a neglectable effect on most of the considered scenarios. Only in short-scale operations such as refueling, minor deviations are visible.

The comparison of the three physical storage technologies has shown that CcH2 allows for the longest discharge periods due to the highest usable density. While CH2 tanks have the lowest usable density, less equipment, such as internal or external heat exchangers, is required and no risk of venting during dormancy scenarios exists. As a further comparison of CcH2 and sLH2 showed, more heat flow needs to be added to CcH2 tanks by the internal heat exchanger during discharge to not fall below a minimum system pressure. sLH2 thereby uses the advantage of the two-phase region: here, less heat flow is required to keep a certain pressure since the hydrogen only needs to be evaporated instead of being heated.

When comparing CcH2 and sLH2 in terms of dormancy behavior, CcH2 has shown to be advantageous for the considered simulation parameters and starting conditions as venting starts later, the venting mass flow rate stays lower, and even in extremely long dormancy scenarios, still a significant amount of hydrogen stays within the tank. However, this significantly depends on the design characteristics, such as fill and maximum pressure.

While the presented model can simulate all operating modes and scenarios of the three considered hydrogen storage tanks, all investigated studies assume idealized drive cycles with constant mass flow rates and perfectly controllable inner heat exchangers. Therefore, in future works, more realistic drive cycles will be studied, using nonconstant mass flow rates and considering prototype data for model validation. These further investigations will then be applied to finding optimal operating strategies. Thereby, the modularized structure of the model, including three operating scenarios and three operational modes, will allow for easy adaption of the considered simulation problem. Additionally, more detailed studies on the separate components,

such as the heat exchangers, should be conducted. By studying these more complex systems, strategies for avoiding venting during dormancy or smart control strategies for the heat exchangers can be investigated. Furthermore, the overall thermal management system could be optimized, e.g., by considering utilization of the cold energy of the sLH2 and CcH2 as suggested by Yang et al. [69].

CRediT authorship contribution statement

Laura Stops: Writing – original draft, Validation, Methodology, Investigation, Conceptualization. **Daniel Siebe:** Writing – review & editing, Validation, Investigation, Conceptualization. **Alexander Stary:** Writing – review & editing, Validation, Investigation, Conceptualization. **Johannes Hamacher:** Writing – review & editing, Validation, Investigation, Conceptualization. **Valeria Sidarava:** Writing – review & editing, Validation, Investigation. **Sebastian Rehfeldt:** Writing – review & editing, Validation, Project administration, Funding acquisition. **Harald Klein:** Writing – review & editing, Validation, Supervision, Resources, Methodology, Conceptualization.

Declaration of competing interest

The authors declare that they have no known competing financial interests or personal relationships that could have appeared to influence the work reported in this paper.

Data availability

No data was used for the research described in the article.

Acknowledgements

Appendix A. Detailed derivations

In this section, additional derivations are provided.

A.1. Derivation of the explicit energy balance

First, the explicit energy balance for the single-phase region (Equation (5)) is derived stepwise, starting from the balance of the internal energy U of the hydrogen in Equation (2). For simplification, in this derivation not the actual indices of the mass and heat flows as labeled in the main part of the paper are used. Instead, all streams flowing into the considered system are named "in" and all streams flowing out of the considered system are named "out". Thus, for the hydrogen control volume, the heat flow from the solid and from the internal heat exchanger are summarized: $\dot{Q}_{in} = \dot{Q}_s + \dot{Q}_{disch}$. Furthermore, the mass flows can be written as $\dot{M}_{in} = \dot{M}_{fuel}$ and $\dot{M}_{out} = \dot{M}_{disch} + \dot{M}_{vent}$.

As a result, the mass balance in this derivation can be simplified to

$$\frac{\mathrm{d}M}{\mathrm{d}t} = \dot{M}_{in} - \dot{M}_{out} \ . \tag{A.1}$$

In a first derivation step, the internal energy and its derivative are expressed by the hydrogen mass M and the specific internal energy u in Equation (A.2) and Equation (A.3):

$$U = M \cdot u \tag{A.2}$$

$$\frac{\mathrm{d}U}{\mathrm{d}t} = M \cdot \frac{\mathrm{d}u}{\mathrm{d}t} + u \cdot \frac{\mathrm{d}M}{\mathrm{d}t} \ . \tag{A.3}$$

With Equation (A.3), $\frac{\mathrm{d}M}{\mathrm{d}t}$ following from the mass balance (Equation (A.1)), and $u = h - p \cdot v$ following from the definition of the specific

enthalpy h, the energy balance can be rephrased to Equation (A.4) and rearranged to Equation (A.5). Thereby, p is the pressure, v the specific volume, and h the specific enthalpy:

$$M \cdot \frac{\mathrm{d}u}{\mathrm{d}t} + \left(\dot{M}_{\text{in}} - \dot{M}_{\text{out}} \right) \cdot (h - p \cdot v)$$
$$= \dot{M}_{\text{in}} \cdot h_{\text{in}} - \dot{M}_{\text{out}} \cdot h_{\text{out}} + \dot{Q}_{\text{in}} \tag{A.4}$$

$$M \cdot \frac{\mathrm{d}u}{\mathrm{d}t} = \dot{M}_{\text{in}} \cdot (h_{\text{in}} - h) - \dot{M}_{\text{out}} \cdot (h_{\text{out}} - h)$$
$$+ \left(\dot{M}_{\text{in}} - \dot{M}_{\text{out}} \right) \cdot p \cdot v + \dot{Q}_{\text{in}} . \tag{A.5}$$

Then, the caloric equation of state is used to further break down the differential specific internal energy [70, p. 212]:

$$\frac{\mathrm{d}u}{\mathrm{d}t} = c_v \cdot \frac{\mathrm{d}T}{\mathrm{d}t} + \left[T \cdot \left(\frac{\partial p}{\partial T} \right)_v - p \right] \cdot \frac{\mathrm{d}v}{\mathrm{d}t}$$
$$= c_v \cdot \frac{\mathrm{d}T}{\mathrm{d}t} - \frac{1}{\varrho^2} \cdot \left[T \cdot \left(\frac{\partial p}{\partial T} \right)_\varrho - p \right] \cdot \frac{\mathrm{d}\varrho}{\mathrm{d}t} . \tag{A.6}$$

Thereby, c_v is the specific isochoric heat capacity and ϱ is the density, with $M = \varrho \cdot V_{\text{tank}}$. By inserting Equation (A.6) into Equation (A.5), the left side of the energy balance can be written as

$$M \cdot \left(c_v \cdot \frac{\mathrm{d}T}{\mathrm{d}t} - \frac{1}{\varrho^2} \cdot \left[T \cdot \left(\frac{\partial p}{\partial T} \right)_v - p \right] \cdot \frac{\mathrm{d}\varrho}{\mathrm{d}t} \right)$$
$$= M \cdot c_v \cdot \frac{\mathrm{d}T}{\mathrm{d}t} - \frac{V_{\text{tank}}}{\varrho} \cdot \left[T \cdot \left(\frac{\partial p}{\partial T} \right)_\varrho - p \right] \cdot \frac{\mathrm{d}\varrho}{\mathrm{d}t} . \tag{A.7}$$

With $\frac{\mathrm{d}\varrho}{\mathrm{d}t} = \frac{1}{V_{\text{tank}}} \cdot \frac{\mathrm{d}M}{\mathrm{d}t}$ and Equation (A.1), the left side of the energy balance in Equation (A.7) is further reformulated to

$$M \cdot c_v \cdot \frac{\mathrm{d}T}{\mathrm{d}t} - \frac{V_{\text{tank}}}{\varrho} \cdot \left[T \cdot \left(\frac{\partial p}{\partial T} \right)_\varrho - p \right] \cdot \frac{1}{V_{\text{tank}}} \cdot \left(\dot{M}_{\text{in}} - \dot{M}_{\text{out}} \right)$$
$$= M \cdot c_v \cdot \frac{\mathrm{d}T}{\mathrm{d}t} - \left(\dot{M}_{\text{in}} - \dot{M}_{\text{out}} \right) \cdot \left[\frac{T}{\varrho} \cdot \left(\frac{\partial p}{\partial T} \right)_\varrho - p \cdot v \right] . \tag{A.8}$$

Inserting the reformulated left-hand side of the energy balance (Equation (A.8)) into Equation (A.5), results in

$$M \cdot c_v \cdot \frac{\mathrm{d}T}{\mathrm{d}t} - \left(\dot{M}_{\text{in}} - \dot{M}_{\text{out}} \right) \cdot \left[\frac{T}{\varrho} \cdot \left(\frac{\partial p}{\partial T} \right)_\varrho - p \cdot v \right]$$
$$= \dot{M}_{\text{in}} \cdot (h_{\text{in}} - h) - \dot{M}_{\text{out}} \cdot (h_{\text{out}} - h)$$
$$+ \left(\dot{M}_{\text{in}} - \dot{M}_{\text{out}} \right) \cdot p \cdot v + \dot{Q}_{\text{in}} . \tag{A.9}$$

Rearranging Equation (A.9) finally leads to the following explicit differential equation for the temperature in the single-phase region:

$$M \cdot c_v \cdot \frac{\mathrm{d}T}{\mathrm{d}t}$$
$$= \left(\dot{M}_{\text{in}} - \dot{M}_{\text{out}} \right) \cdot \frac{T}{\varrho} \cdot \left(\frac{\partial p}{\partial T} \right)_\varrho$$
$$+ \dot{M}_{\text{in}} \cdot (h_{\text{in}} - h) - \dot{M}_{\text{out}} \cdot (h_{\text{out}} - h) + \dot{Q}_{\text{in}} . \tag{A.10}$$

By inserting the actual mass flow rates, corresponding enthalpies, and heat flows for venting, refueling, and discharge, the model's explicit differential equation for the temperature (Equation (5)) results.

A.2. Derivation of the two-phase energy balance

To formulate the explicit energy balance for the two-phase region, REFPROP's [2] property c_{v2P} is used. It can be understood as a generic specific isochoric two-phase heat capacity and is defined in a way that allows similar usage as specific isochoric single-phase heat capacities. However, its physical meaning goes beyond and is derived in Appendix A.3.

For describing the two-phase region, the vapor fraction x is decisive. It is defined as follows by the mass of the gas M'' or the liquid M' related to the overall mass M:

$$x = \frac{M''}{M} \quad \to \quad 1 - x = \frac{M'}{M} . \tag{A.11}$$

The specific state variables, such as internal energy u and volume v now can be expressed using the vapor fraction and the respective property of the saturated liquid ($'$) or gas ($''$):

$$u = (1 - x) \cdot u' + x \cdot u'' = u' + x \cdot (u'' - u') = u' + x \cdot \Delta u \tag{A.12}$$

$$v = (1 - x) \cdot v' + x \cdot v'' = v' + x \cdot (v'' - v') = v' + x \cdot \Delta v . \tag{A.13}$$

Then, the differential specific internal energy $\mathrm{d}u$ is written as

$$\mathrm{d}u = (1 - x) \cdot \mathrm{d}u' + x \cdot \mathrm{d}u'' - u' \cdot \mathrm{d}x + u'' \cdot \mathrm{d}x$$
$$= (1 - x) \cdot \mathrm{d}u' + x \cdot \mathrm{d}u'' + \Delta u \cdot \mathrm{d}x . \tag{A.14}$$

In a next step, the vapor fraction can be expressed by the specific internal energy or the specific volume as follows:

$$x = \frac{u - u'}{u'' - u'} = \frac{v - v'}{v'' - v'} . \tag{A.15}$$

Thus, the differential change of the vapor fraction $\mathrm{d}x$ can be written as:

$$\mathrm{d}x = \frac{(\mathrm{d}v - \mathrm{d}v') \cdot (v'' - v') - (v - v') \cdot (\mathrm{d}v'' - \mathrm{d}v')}{(v'' - v')^2}$$
$$= \frac{\mathrm{d}v}{\Delta v} - \frac{\mathrm{d}v'}{\Delta v} - \frac{x}{\Delta v} \cdot (\mathrm{d}v'' - \mathrm{d}v')$$
$$= \frac{\mathrm{d}v}{\Delta v} - \frac{1}{\Delta v} \cdot \left[(1 - x) \cdot \mathrm{d}v' + x \cdot \mathrm{d}v'' \right] . \tag{A.16}$$

Inserting Equation (A.16) into Equation (A.14) then leads to

$$\mathrm{d}u = (1 - x) \cdot \mathrm{d}u' + x \cdot \mathrm{d}u''$$
$$+ \frac{\Delta u}{\Delta v} \cdot \left(\mathrm{d}v - \left((1 - x) \cdot \mathrm{d}v' + x \cdot \mathrm{d}v'' \right) \right) . \tag{A.17}$$

Thereby, the term $\frac{\Delta u}{\Delta v}$ can be determined with the Clausius-Clapeyron equation.

Since the model derived in this article assumes vapor-liquid equilibrium in the two-phase region, the Clausius-Clapeyron equation formulated in Equation (A.18) is valid [70, p. 468]:

$$\frac{\mathrm{d}p_{\text{sat}}}{\mathrm{d}T} = \frac{s'' - s'}{v'' - v'} = \frac{h'' - h'}{T \cdot (v'' - v')} = \frac{\Delta h}{T \cdot \Delta v} . \tag{A.18}$$

With $\Delta h = \Delta u + p_{\text{sat}} \cdot \Delta u$, Equation (A.18) can be rearranged to Equation (A.19) and finally Equation (A.20):

$$T \cdot \frac{\mathrm{d}p_{\text{sat}}}{\mathrm{d}T} = \frac{\Delta h}{\Delta v} = \frac{\Delta u + p_{\text{sat}} \cdot \Delta v}{\Delta v} \tag{A.19}$$

$$\frac{\Delta u}{\Delta v} = T \cdot \frac{\mathrm{d}p_{\text{sat}}}{\mathrm{d}T} - p_{\text{sat}} . \tag{A.20}$$

By inserting Equation (A.20) into (A.17), the differential change of the specific internal energy $\mathrm{d}u$ is determined by

$$\mathrm{d}u = (1 - x) \cdot \mathrm{d}u' + x \cdot \mathrm{d}u''$$
$$+ \left(T \cdot \frac{\mathrm{d}p_{\text{sat}}}{\mathrm{d}T} - p_{\text{sat}} \right) \cdot \left(\mathrm{d}v - \left((1 - x) \cdot \mathrm{d}v' + x \cdot \mathrm{d}v'' \right) \right) . \tag{A.21}$$

Equation (A.21) can be considered as the governing caloric equation of state in the two-phase region. Thereby, the differential changes of the specific internal energies at the saturation states, $\mathrm{d}u'$ and $\mathrm{d}u''$, can be determined by Equations (A.22) and (A.23):

$$\mathrm{d}u' = c_v' \cdot \mathrm{d}T + \left[T \cdot \left(\frac{\partial p}{\partial T} \right)_{v'} - p \right] \cdot \mathrm{d}v' \tag{A.22}$$

$$\mathrm{d}u'' = c_v'' \cdot \mathrm{d}T + \left[T \cdot \left(\frac{\partial p}{\partial T} \right)_{v''} - p \right] \cdot \mathrm{d}v'' . \tag{A.23}$$

The starting point for further derivation is the energy balance in Equation (A.5) at $p = p_{sat}$:

$$M \cdot \frac{du}{dt} = \dot{M}_{in} \cdot (h_{in} - h) + \dot{M}_{out} \cdot (h_{out} - h)$$
$$+ (\dot{M}_{in} - \dot{M}_{out}) \cdot p_{sat} \cdot v + \dot{Q}_{in} . \quad (A.24)$$

This equation also includes the single-phase region with $dx = 0$ and $x = 1$ for saturated vapor or $x = 0$ for saturated liquid. With Equation (A.14), the left-hand side can be written as

$$M \cdot \frac{du}{dt} = M \cdot \left[(1-x) \cdot \frac{du'}{dt} + x \cdot \frac{du''}{dt} + \Delta u \cdot \frac{dx}{dt} \right] . \quad (A.25)$$

Now, inserting the correlation for the differential change of the vapor fraction dx (Equation (A.16)) leads to

$$M \cdot \frac{du}{dt} = M \cdot \left[(1-x) \cdot \frac{du'}{dt} + x \cdot \frac{du''}{dt} - \frac{\Delta u}{\Delta v} \cdot \left((1-x) \cdot \frac{dv'}{dt} + x \cdot \frac{dv''}{dt} - \frac{dv}{dt} \right) \right]$$
$$= M \cdot \left[(1-x) \cdot \frac{du'}{dt} + x \cdot \frac{du''}{dt} - \frac{\Delta u}{\Delta v} \cdot \left((1-x) \cdot \frac{dv'}{dt} + x \cdot \frac{dv''}{dt} \right) \right]$$
$$+ M \cdot \frac{\Delta u}{\Delta v} \cdot \frac{dv}{dt} . \quad (A.26)$$

The term $M \cdot \frac{\Delta u}{\Delta v} \cdot \frac{dv}{dt}$ can be further rearranged to Equation (A.27) using Equation (A.20) that follows from the Clausius-Clapeyron correlation. Thereby, also the correlations $v = \frac{1}{\varrho}$, $M = \varrho \cdot V_{tank}$, $V_{tank} \cdot \frac{d\varrho}{dt} = \frac{dM}{dt}$, and $\frac{dM}{dt} = \dot{M}_{in} - \dot{M}_{out}$ are used:

$$M \cdot \frac{\Delta u}{\Delta v} \cdot \frac{dv}{dt} = -\frac{\varrho \cdot V_{tank}}{\varrho^2} \cdot \left(T \cdot \frac{dp_{sat}}{dT} - p_{sat} \right) \cdot \frac{d\varrho}{dt}$$
$$= -\frac{T}{\varrho} \cdot \frac{dp_{sat}}{dT} \cdot (\dot{M}_{in} - \dot{M}_{out}) + p_{sat} \cdot v \cdot (\dot{M}_{in} - \dot{M}_{out}) . \quad (A.27)$$

Replacing the left side of Equation (A.24) with Equation (A.27) results in the term $p_{sat} \cdot v \cdot (\dot{M}_{in} - \dot{M}_{out})$ dropping out. Thus, the following energy balance is obtained:

$$M \cdot \left[(1-x) \cdot \frac{du'}{dt} + x \cdot \frac{du''}{dt} - \frac{\Delta u}{\Delta v} \cdot \left((1-x) \cdot \frac{dv'}{dt} + x \cdot \frac{dv''}{dt} \right) \right]$$
$$= \frac{T}{\varrho} \cdot \frac{dp_{sat}}{dT} \cdot (\dot{M}_{in} - \dot{M}_{out})$$
$$+ \dot{M}_{in} \cdot (h_{in} - h) - \dot{M}_{out} \cdot (h_{out} - h) + \dot{Q}_{in} . \quad (A.28)$$

By formally expanding with dT/dT, the left side of Equation (A.28) can be written as

$$M \cdot \underbrace{\left[(1-x) \cdot \frac{du'}{dT} + x \cdot \frac{du''}{dT} - \frac{\Delta u}{\Delta v} \cdot \left((1-x) \cdot \frac{dv'}{dT} + x \cdot \frac{dv''}{dT} \right) \right]}_{c_{v2P}} \cdot \frac{dT}{dt} .$$

Thereby, the correlation within the brackets can be considered as a specific isochoric two-phase heat capacity c_{v2P} defined as

$$c_{v2P} = (1-x) \cdot \frac{du'}{dT} + x \cdot \frac{du''}{dT} - \frac{\Delta u}{\Delta v} \cdot \left((1-x) \cdot \frac{dv'}{dT} + x \cdot \frac{dv''}{dT} \right)$$
$$= (1-x) \cdot \underbrace{\left(\frac{du'}{dT} - \frac{\Delta u}{\Delta v} \cdot \frac{dv'}{dT} \right)}_{c'_{v2P}} + x \cdot \underbrace{\left(\frac{du''}{dT} - \frac{\Delta u}{\Delta v} \cdot \frac{dv''}{dT} \right)}_{c''_{v2P}}$$
$$= (1-x) \cdot c'_{v2P} + x \cdot c''_{v2P} . \quad (A.29)$$

With Equation (A.20), the specific isochoric two-phase heat capacities c'_{v2P} and c''_{v2P} of the two saturation states are defined as:

$$c'_{v2P} = \frac{du'}{dT} - \frac{\Delta u}{\Delta v} \cdot \frac{dv'}{dT} = \frac{du'}{dT} - \left(T \cdot \frac{dp_{sat}}{dT} - p_{sat} \right) \cdot \frac{dv'}{dT} \quad (A.30)$$

$$c''_{v2P} = \frac{du''}{dT} - \frac{\Delta u}{\Delta v} \cdot \frac{dv''}{dT} = \frac{du''}{dT} - \left(T \cdot \frac{dp_{sat}}{dT} - p_{sat} \right) \cdot \frac{dv''}{dT} . \quad (A.31)$$

Using the definition for c_{v2P} (Equation (A.29)), the energy balance for the two-phase region in Equation (A.28) finally results in Equation (A.32).

$$M \cdot c_{v2P} \cdot \frac{dT}{dt} = \frac{T}{\varrho} \cdot \frac{dp_{sat}}{dT} \cdot (\dot{M}_{in} - \dot{M}_{out})$$
$$+ \dot{M}_{in} \cdot (h_{in} - h) - \dot{M}_{out} \cdot (h_{out} - h) + \dot{Q}_{in} \quad (A.32)$$

By inserting the correct streams for $\dot{M}_{in}$ and $\dot{M}_{out}$, the corresponding specific enthalpies, and the correct streams for $\dot{Q}_{in}$ for venting, refueling, and discharge, the model's explicit differential equation for the temperature in the two-phase region (Equation (12)) is derived.

In the model, c'_{v2P} and c''_{v2P} can be calculated with REFPROP [2]. However, the definition is not fully documented. In Span [71, p. 44], a correlation for a specific isochoric heat capacity in the two-phase region is given, using a partial derivative of the specific entropy s. Hereafter, it is shown how this correlation can be derived from the definition in Equation (A.30). Furthermore, as partial derivatives of the specific entropy are not available in the REFPROP [2] graphical user interface, the correlations for c'_{v2P} and c''_{v2P} are further dissembled to derive thermodynamic equations for their calculation and provide proper documentation for the definition of c_{v2P}.

A.3. Specific isochoric two-phase heat capacities c'_{v2P} and c''_{v2P}

In this section, the definitions of c'_{v2P} and c''_{v2P} are further examined. Additionally, equations to calculate the specific isochoric two-phase heat capacities c'_{v2P} and c''_{v2P} with REFPROP [2] are derived. Since the definition of c''_{v2P} is analogous to the definition of c'_{v2P}, in the following, only the latter one is considered in detail.

As derived in the previous section, c'_{v2P} is defined by Equation (A.33).

$$c'_{v2P} = \frac{du'}{dT} - \left(T \cdot \frac{dp_{sat}}{dT} - p_{sat} \right) \cdot \frac{dv'}{dT} \quad (A.33)$$

To show that c'_{v2P} is a specific isochoric heat capacity, the fundamental equation for the specific liquid internal energy [70, p.247],

$$du' = T \cdot ds' - p_{sat} \cdot dv' , \quad (A.34)$$

is inserted into Equation (A.33), resulting in

$$c'_{v2P} = T \cdot \frac{ds'}{dT} - p_{sat} \cdot \frac{dv'}{dT} - \left(T \cdot \frac{dp_{sat}}{dT} - p_{sat} \right) \cdot \frac{dv'}{dT}$$
$$= T \cdot \left(\frac{ds'}{dT} - \frac{dp_{sat}}{dT} \cdot \frac{dv'}{dT} \right) . \quad (A.35)$$

With $s' = s'(T, v')$ and the resulting total differential for the specific entropy at saturated liquid state s', the term $\frac{ds'}{dT}$ can be written as:

$$\frac{ds'}{dT} = \left(\frac{\partial s'}{\partial T} \right)_{v'} + \left(\frac{\partial s'}{\partial v'} \right)_T \cdot \frac{dv'}{dT} . \quad (A.36)$$

Inserting this correlation into Equation (A.35) results in

$$c'_{v2P} = T \cdot \left[\left(\frac{\partial s'}{\partial T} \right)_{v'} + \left(\frac{\partial s'}{\partial v'} \right)_T \cdot \frac{dv'}{dT} - \frac{dp_{sat}}{dT} \cdot \frac{dv'}{dT} \right] . \quad (A.37)$$

According to Thorade and Saadat [72], within the two-phase region, derivatives at constant temperature can be written as shown in Equation (A.38) for the partial derivative of the specific entropy in the direction of the specific volume:

$$\left(\frac{\partial s'}{\partial v'} \right)_T = \left(\frac{\partial s''}{\partial v''} \right)_T = \frac{s'' - s'}{v'' - v'} . \quad (A.38)$$

Thus, with the Clausius-Clapeyron correlation (Equation (A.18)), the following correlation is obtained:

$$\left(\frac{\partial s'}{\partial v'}\right)_T = \frac{\mathrm{d}p_{\mathrm{sat}}}{\mathrm{d}T} \ . \tag{A.39}$$

As a result, inserting Equation (A.39) into Equation (A.37) leads to

$$c'_{v2P} = T \cdot \left(\frac{\partial s'}{\partial T}\right)_{v'} \ , \tag{A.40}$$

which is the generalized form to determine the specific isochoric heat capacity from the derivative of the specific entropy and corresponds with Span [71, p. 44].

Since $\left(\frac{\partial s'}{\partial T}\right)_{v'}$ is not directly accessible using the REFPROP [2] graphical user interface, a correlation only depending on accessible variables and derivatives is derived hereafter, starting from Equation (A.33). With $u' = u'(T, v')$ and the total differential, the differential change of the internal energy with temperature along the saturation line $\frac{\mathrm{d}u'}{\mathrm{d}T}$ is written as

$$\frac{\mathrm{d}u'}{\mathrm{d}T} = \left(\frac{\partial u'}{\partial T}\right)_{v'} + \left(\frac{\partial u'}{\partial v'}\right)_T \cdot \frac{\mathrm{d}v'}{\mathrm{d}T} \ . \tag{A.41}$$

Using Equation (A.22), $\frac{\mathrm{d}u'}{\mathrm{d}T}$ can also be written as:

$$\frac{\mathrm{d}u'}{\mathrm{d}T} = c'_v + \left[T \cdot \left(\frac{\partial p}{\partial T}\right)_{v'} - p_{\mathrm{sat}}\right] \cdot \frac{\mathrm{d}v'}{\mathrm{d}T} \ . \tag{A.42}$$

By inserting Equation (A.42) into Equation (A.33), the following correlation for c'_{v2P} is obtained:

$$c'_{v2P} = c'_v + \left[T \cdot \left(\frac{\partial p}{\partial T}\right)_{v'} - p_{\mathrm{sat}}\right] \cdot \frac{\mathrm{d}v'}{\mathrm{d}T} - \left(T \cdot \frac{\mathrm{d}p_{\mathrm{sat}}}{\mathrm{d}T} - p_{\mathrm{sat}}\right) \cdot \frac{\mathrm{d}v'}{\mathrm{d}T}$$

$$= c'_v + T \cdot \left[\left(\frac{\partial p}{\partial T}\right)_{v'} - \frac{\mathrm{d}p_{\mathrm{sat}}}{\mathrm{d}T}\right] \cdot \frac{\mathrm{d}v'}{\mathrm{d}T} \ . \tag{A.43}$$

For a saturated liquid, $\frac{\mathrm{d}v'}{\mathrm{d}T}$, which equals the change of the specific volume with temperature along the saturation line, is always positive. Further, the partial derivative of the pressure in the direction of the temperature at the saturation line $\left(\frac{\partial p}{\partial T}\right)_{v'}$ is larger than the change of the saturation pressure with temperature $\frac{\mathrm{d}p_{\mathrm{sat}}}{\mathrm{d}T}$. As a result, Equation (A.43) shows that c'_{v2P} is always larger than c'_v. When, instead saturated gas is considered, $\frac{\mathrm{d}v''}{\mathrm{d}T}$ is always negative. However, since $\left(\frac{\partial p}{\partial T}\right)_{v'}$ is smaller than $\frac{\mathrm{d}p_{\mathrm{sat}}}{\mathrm{d}T}$, also c''_{v2P} is always larger than c''_v.

To further break down Equation (A.43), the total differential can be used to write $\frac{\mathrm{d}v'}{\mathrm{d}T}$ as

$$\frac{\mathrm{d}v'}{\mathrm{d}T} = \left(\frac{\partial v'}{\partial T}\right)_p + \left(\frac{\partial v'}{\partial p}\right)_T \cdot \frac{\mathrm{d}p_{\mathrm{sat}}}{\mathrm{d}T} \ . \tag{A.44}$$

Inserting Equation (A.44) into Equation (A.43) finally leads to

$$c'_{v2P} = c'_v + T \cdot \left[\left(\frac{\partial p}{\partial T}\right)_{v'} - \frac{\mathrm{d}p_{\mathrm{sat}}}{\mathrm{d}T}\right] \cdot \left[\left(\frac{\partial v'}{\partial T}\right)_p + \left(\frac{\partial v'}{\partial p}\right)_T \cdot \frac{\mathrm{d}p_{\mathrm{sat}}}{\mathrm{d}T}\right] \ . \tag{A.45}$$

In a last step, $\varrho = \frac{1}{v}$ can be inserted to find the final form of the correlation for c'_{v2P}:

$$c'_{v2P} = c'_v - \frac{T}{\varrho'^2} \cdot \left[\left(\frac{\partial p}{\partial T}\right)_{\varrho'} - \frac{\mathrm{d}p_{\mathrm{sat}}}{\mathrm{d}T}\right]$$

$$\cdot \left[\left(\frac{\partial \varrho'}{\partial T}\right)_p - \left(\frac{\partial \varrho'}{\partial p}\right)_T \cdot \frac{\mathrm{d}p_{\mathrm{sat}}}{\mathrm{d}T}\right] \ . \tag{A.46}$$

When considering the specific isochoric two-phase heat capacity c''_{v2P} the derivation is analogous and will result in

$$c''_{v2P} = c''_v - \frac{T}{\varrho''^2} \cdot \left[\left(\frac{\partial p}{\partial T}\right)_{\varrho''} - \frac{\mathrm{d}p_{\mathrm{sat}}}{\mathrm{d}T}\right]$$

$$\cdot \left[\left(\frac{\partial \varrho''}{\partial T}\right)_p - \left(\frac{\partial \varrho''}{\partial p}\right)_T \cdot \frac{\mathrm{d}p_{\mathrm{sat}}}{\mathrm{d}T}\right] \ . \tag{A.47}$$

Finally, the specific isochoric two-phase heat capacity c_{v2P} can be calculated from c'_{v2P} and c''_{v2P} with Equation (A.29). Thereby the same results are obtained whether calculating c'_{v2P} and c''_{v2P} with Equation (A.46) and Equation (A.47) or using REFPROP [2] calls to calculate c'_{v2P} and c''_{v2P} directly.

A.4. Derivation of the required discharge heat flow

Within this section, the equation for the discharge heat flow $\dot{Q}_{\mathrm{disch}}$ (Equation (22)), that is required for keeping the minimum system pressure, is derived. In this scenario, the pressure of the hydrogen is constant ($p = p_{\mathrm{min}} = \mathrm{const}$) and the internal heat exchanger is switched on.

In the discharge case, Equation (A.10) is reformulated to

$$M \cdot c_v \cdot \frac{\mathrm{d}T}{\mathrm{d}t} = -\dot{M}_{\mathrm{disch}} \cdot \frac{T}{\varrho} \cdot \left(\frac{\partial p}{\partial T}\right)_{\varrho}$$

$$- \dot{M}_{\mathrm{disch}} \cdot \left(h_{\mathrm{disch}} - h\right) + \dot{Q}_{\mathrm{disch}} + \dot{Q}_{\mathrm{s}} \ . \tag{A.48}$$

By rearranging Equation (A.48), a correlation for $\dot{Q}_{\mathrm{disch}}$ is found:

$$\dot{Q}_{\mathrm{disch}} = M \cdot c_v \cdot \frac{\mathrm{d}T}{\mathrm{d}t} + \dot{M}_{\mathrm{disch}} \cdot \left[\frac{T}{\varrho} \cdot \left(\frac{\partial p}{\partial T}\right)_{\varrho} + \left(h_{\mathrm{disch}} - h\right)\right] - \dot{Q}_{\mathrm{s}} \ . \tag{A.49}$$

With the total differential of the temperature,

$$\frac{\mathrm{d}T}{\mathrm{d}t} = \left(\frac{\partial T}{\partial p}\right)_{\varrho} \cdot \frac{\mathrm{d}p}{\mathrm{d}t} + \left(\frac{\partial T}{\partial \varrho}\right)_p \cdot \frac{\mathrm{d}\varrho}{\mathrm{d}t}, \tag{A.50}$$

and isobaric conditions ($\frac{\mathrm{d}p}{\mathrm{d}t} = 0$) when the internal heat exchanger is switched on to keep the pressure, $\frac{\mathrm{d}T}{\mathrm{d}t}$ can be written as

$$\frac{\mathrm{d}T}{\mathrm{d}t} = \left(\frac{\partial T}{\partial \varrho}\right)_p \cdot \frac{\mathrm{d}\varrho}{\mathrm{d}t}$$

$$= \frac{1}{V_{\mathrm{tank}}} \cdot \left(\frac{\partial T}{\partial \varrho}\right)_p \cdot \left(-\dot{M}_{\mathrm{disch}}\right) \ . \tag{A.51}$$

When inserting Equation (A.51) into Equation (A.49), the following equation is derived which corresponds to Equation (22) in Section 2:

$$\dot{Q}_{\mathrm{disch}} = \dot{M}_{\mathrm{disch}} \cdot \left[\frac{T}{\varrho} \cdot \left(\frac{\partial p}{\partial T}\right)_{\varrho} + \left(h_{\mathrm{disch}} - h\right) - \varrho \cdot c_v \cdot \left(\frac{\partial T}{\partial \varrho}\right)_p\right] - \dot{Q}_{\mathrm{s}} \ . \tag{A.52}$$

For the two-phase region, the correlation for the required heat flow $\dot{Q}_{\mathrm{disch}}$ to keep the pressure can be derived analogously to the single-phase region by reformulating Equation (12) for the minimum pressure case:

$$M \cdot c_{v2P} \cdot \frac{\mathrm{d}T}{\mathrm{d}t} = -\dot{M}_{\mathrm{disch}} \cdot \frac{T}{\varrho} \cdot \frac{\mathrm{d}p_{\mathrm{sat}}}{\mathrm{d}T}$$

$$- \dot{M}_{\mathrm{disch}} \cdot \left(h_{\mathrm{disch}} - h\right) + \dot{Q}_{\mathrm{disch}} + \dot{Q}_{\mathrm{s}} \ . \tag{A.53}$$

Since in the two-phase region, $\frac{\mathrm{d}T}{\mathrm{d}t} = 0$ when $\frac{\mathrm{d}p}{\mathrm{d}t} = 0$, the equation can be simplified and Equation (23) in Section 2 is derived:

$$\dot{Q}_{\mathrm{disch}} = \dot{M}_{\mathrm{disch}} \cdot \left[\frac{T}{\varrho} \cdot \frac{\mathrm{d}p_{\mathrm{sat}}}{\mathrm{d}T} + \left(h_{\mathrm{disch}} - h\right)\right] - \dot{Q}_{\mathrm{s}} \ . \tag{A.54}$$

A.5. Derivation of venting mass flow

The equation for the venting mass flow $\dot{M}_{\mathrm{vent}}$ (Equation (26)) that is required for keeping the maximum system pressure by venting is de-

rived in this section. When hydrogen is vented from the tank during dormancy, $p = p_{\text{vent}} = \text{const}$ is valid.

In the dormancy case, Equation (A.10) is reformulated to

$$M \cdot c_v \cdot \frac{dT}{dt} = -\dot{M}_{\text{vent}} \cdot \frac{T}{\varrho} \cdot \left(\frac{\partial p}{\partial T}\right)_\varrho - \dot{M}_{\text{vent}} \cdot (h_{\text{vent}} - h) + \dot{Q}_s \ . \quad \text{(A.55)}$$

Again, with the total differential

$$\frac{dT}{dt} = \left(\frac{\partial T}{\partial p}\right)_\varrho \cdot \frac{dp}{dt} + \left(\frac{\partial T}{\partial \varrho}\right)_p \cdot \frac{d\varrho}{dt} \quad \text{(A.56)}$$

and $\frac{dp}{dt} = 0$ in the venting case, $\frac{dT}{dt}$ can be simplified to

$$\frac{dT}{dt} = \left(\frac{\partial T}{\partial \varrho}\right)_p \cdot \frac{d\varrho}{dt}$$
$$= \frac{1}{V_{\text{tank}}} \cdot \left(\frac{\partial T}{\partial \varrho}\right)_p \cdot (-\dot{M}_{\text{vent}}) \ . \quad \text{(A.57)}$$

By inserting Equation (A.57) into Equation (A.55) and solving for $\dot{M}_{\text{vent}}$, the following equation is derived, which corresponds to Equation (26) in Section 2:

$$\dot{M}_{\text{vent}} = \frac{\dot{Q}_s}{\frac{T}{\varrho} \cdot \left(\frac{\partial p}{\partial T}\right)_\varrho + (h_{\text{vent}} - h) - \varrho \cdot c_v \cdot \left(\frac{\partial T}{\partial \varrho}\right)_p} \ . \quad \text{(A.58)}$$

For the two-phase region, the equation for $\dot{M}_{\text{vent}}$ can be derived analogously to the single-phase region by reformulating Equation (12) for the dormancy scenario:

$$M \cdot c_{v2P} \cdot \frac{dT}{dt} = -\dot{M}_{\text{vent}} \cdot \frac{T}{\varrho} \cdot \frac{dp_{\text{sat}}}{dT} - \dot{M}_{\text{vent}} \cdot (h_{\text{vent}} - h) + \dot{Q}_s \ . \quad \text{(A.59)}$$

Again, in the two-phase region $\frac{dT}{dt} = 0$ is valid since $\frac{dp}{dt} = 0$. Thus, the equation can be simplified as follows, resulting in the equation for $\dot{M}_{\text{vent}}$ (Equation (27) in Section 2):

$$\dot{M}_{\text{vent}} = \frac{\dot{Q}_s}{\frac{T}{\varrho} \cdot \left(\frac{\partial p}{\partial T}\right)_\varrho + (h_{\text{vent}} - h)} \ . \quad \text{(A.60)}$$

References

[1] Hamacher J, Stary A, Stops L, Siebe D, Kapp M, Rehfeldt S, et al. Modeling the thermodynamic behavior of cryo-compressed hydrogen tanks for trucks. Cryogenics 2023;135:103743. https://doi.org/10.1016/j.cryogenics.2023.103743.

[2] Lemmon EW, Bell IH, Huber ML, McLinden M. Nist reference fluid thermodynamic and transport properties database (REFPROP) version 10 - SRD 23; 2018. https://pages.nist.gov/refprop-docs/. [Accessed 30 November 2023].

[3] European Commission. The European green deal. https://ec.europa.eu/commission/presscorner/detail/en/ip_19_6691. [Accessed 30 November 2023]; 2019.

[4] United Nations. The Paris agreement. https://treaties.un.org/pages/ViewDetails.aspx?src=TREATY%26mtdsg_no=XXVII-7-d%26chapter=27%26clang=_en. [Accessed 30 November 2023]; 2015.

[5] Bundesministerium für Umwelt. Naturschutz und nukleare Sicherheit, Bundes-Klimaschutzgesetz. https://www.bmuv.de/themen/klimaschutz-anpassung/klimaschutz/bundes-klimaschutzgesetz. [Accessed 30 November 2023]; 2021.

[6] Klell M, Eichlseder H, Trattner A. Wasserstoff in der Fahrzeugtechnik. Wiesbaden, Wiesbaden: Springer Fachmedien; 2018.

[7] Ajanovic A, Haas R. Prospects and impediments for hydrogen and fuel cell vehicles in the transport sector. Int J Hydrog Energy 2021;46:10049–58. https://doi.org/10.1016/j.ijhydene.2020.03.122.

[8] de de Troya JJ, Álvarez C, Fernández-Garrido C, Carral L. Analysing the possibilities of using fuel cells in ships. Int J Hydrog Energy 2016;41:2853–66. https://doi.org/10.1016/j.ijhydene.2015.11.145.

[9] Baroutaji A, Wilberforce T, Ramadan M, Olabi AG. Comprehensive investigation on hydrogen and fuel cell technology in the aviation and aerospace sectors. Renew Sustain Energy Rev 2019;106:31–40. https://doi.org/10.1016/j.rser.2019.02.022.

[10] Kubota Y. Toyota's fuel-cell car Mirai goes on sale. https://www.wsj.com/articles/BL-JRTB-18738. [Accessed 30 November 2023]; 2014.

[11] Hyundai Motor Group. Hyundai ix35 fuel cell: release. https://www.hyundai.com/worldwide/en/company/newsroom/hyundai-ix35-fuel-cell-0000001596. [Accessed 30 November 2023]; 2013.

[12] Norled AS. MF hydra sails on zero-emission liquid hydrogen. https://www.norled.no/en/news/the-mf-hydra-first-in-the-world/. [Accessed 30 November 2023]; 2023.

[13] ZeroAvia. World first hydrogen-electric passenger plane flight. https://www.zeroavia.com/press-release-25-09-2020. [Accessed 30 November 2023]; 2020.

[14] Airbus SAS. Hydrogen - an energy carrier to fuel the climate-neutral aviation of tomorrow. https://www.airbus.com/innovation/zero-emission/hydrogen. [Accessed 30 November 2023]; 2021.

[15] European Environment Agency. EEA greenhouse gases: data viewer. https://www.eea.europa.eu/data-and-maps/data/data-viewers/greenhouse-gases-viewer. [Accessed 30 November 2023]; 2021.

[16] Volkswagen AG. Nachhaltigkeitsbericht. https://www.volkswagen-group.com/de/publikationen/unternehmensberichte/nachhaltigkeitsbericht-2021-1666. [Accessed 30 November 2023]; 2021.

[17] BMW Group. BMW Group Report. https://www.press.bmwgroup.com/global/article/detail/T0374217EN/bmw-group-report-2021?language=en. [Accessed 30 November 2023]; 2021.

[18] Sagaria S, Costa Neto R, Baptista P. Assessing the performance of vehicles powered by battery, fuel cell and ultra-capacitor: application to light-duty vehicles and buses. Energy Convers Manag 2021;229:113767. https://doi.org/10.1016/j.enconman.2020.113767.

[19] Cano ZP, Banham D, Ye S, Hintennach A, Lu J, Fowler M, et al. Batteries and fuel cells for emerging electric vehicle markets. Nat Energy 2018;3:279–89. https://doi.org/10.1038/s41560-018-0108-1.

[20] Basma H, Beys Y, Rodriguez F. Battery electric tractor-trailers in the European Union: a vehicle technology analysis. International Council on Clean Transportation; 2021.

[21] Thomas CE. Fuel cell and battery electric vehicles compared. Int J Hydrog Energy 2009;34:6005–20. https://doi.org/10.1016/j.ijhydene.2009.06.003.

[22] H2Mobility. Overview hydrogen refuelling for heavy duty vehicles. https://h2-mobility.de/en/hydrogen-refuelling-for-heavy-duty-vehicles/. [Accessed 30 November 2023]; 2021.

[23] Bundesministerium für Wirtschaft und Energie. Die Nationale Wasserstoffstrategie. https://www.bmbf.de/bmbf/de/forschung/energiewende-und-nachhaltiges-wirtschaften/nationale-wasserstoffstrategie/nationale-wasserstoffstrategie_node.html. [Accessed 30 November 2023]; 2020.

[24] Hyundai Truck & Bus. XCIENT fuel cell. https://trucknbus.hyundai.com/hydrogen/en. [Accessed 30 November 2023]; 2022.

[25] Daimler Truck AG. Development milestone: Daimler truck tests fuel-cell truck with liquid hydrogen. https://www.daimlertruck.com/en/newsroom/pressrelease/development-milestone-daimler-truck-tests-fuel-cell-truck-with-liquid-hydrogen-51975637. [Accessed 30 November 2023]; 2022.

[26] Schäfer P. Cryomotive entwickelt Cryogas-Tanks für schwere H2-Lkw. https://www.springerprofessional.de/kraftstoffanlage--tank/wasserstoff/cryomotive-entwickelt-cryogas-tanks-fuer-schwere-h2-lkw/20091304. [Accessed 30 November 2023]; 2022.

[27] Hassan IA, Ramadan HS, Saleh MA, Hissel D. Hydrogen storage technologies for stationary and mobile applications: review, analysis and perspectives. Renew Sustain Energy Rev 2021;149:111311. https://doi.org/10.1016/j.rser.2021.111311.

[28] Rivard E, Trudeau M, Zaghib K. Hydrogen storage for mobility: a review. Materials (Basel, Switzerland) 2019;12. https://doi.org/10.3390/ma12121973.

[29] Baetcke L, Kaltschmitt M. Hydrogen storage for mobile application: technologies and their assessment. In: Hydrogen supply chains. Elsevier; 2018. p. 167–206.

[30] Leachman JW, Jacobsen RT, Penoncello SG, Lemmon EW. Fundamental equations of state for parahydrogen, normal hydrogen, and orthohydrogen. J Phys Chem Ref Data 2009;38:721–48. https://doi.org/10.1063/1.3160306.

[31] Brunner TC, Kampitsch M, Kircher O. Cryo-compressed hydrogen storage. In: Stolten D, Samsun RC, Garland N, editors. Fuel cells: data, facts and figures. Weinheim, Germany: Wiley-VCH Verlag GmbH & Co. KGaA; 2016. p. 162–73.

[32] von Helmolt R, Eberle U. Fuel cell vehicles: status 2007. J Power Sources 2007;165:833–43. https://doi.org/10.1016/j.jpowsour.2006.12.073.

[33] de Miguel N, Ortiz Cebolla R, Acosta B, Moretto P, Harskamp F, Bonato C. Compressed hydrogen tanks for on-board application: thermal behaviour during cycling. Int J Hydrog Energy 2015;40:6449–58. https://doi.org/10.1016/j.ijhydene.2015.03.035.

[34] Magneville B, Gentilleau B, Villalonga S, Nony F, Galiano H. Modeling, parameters identification and experimental validation of composite materials behavior law used in 700 bar type IV hydrogen high pressure storage vessel. Int J Hydrog Energy 2015;40:13193–205. https://doi.org/10.1016/j.ijhydene.2015.06.121.

[35] Ahluwalia RK, Roh H-S, Peng J-K, Papadias D, Baird AR, Hecht ES, et al. Liquid hydrogen storage system for heavy duty trucks: configuration, performance, cost, and safety. Int J Hydrog Energy 2023;48:13308–23. https://doi.org/10.1016/j.ijhydene.2022.12.152.

[36] Krainz G. Development of automotive liquid hydrogen storage systems. In: AIP conference proceedings. AIP; 2004. p. 35–40.

[37] Moreno-Blanco J, Petitpas G, Espinosa-Loza F, Elizalde-Blancas F, Martinez-Frias J, Aceves SM. The fill density of automotive cryo-compressed hydrogen vessels. Int J Hydrog Energy 2019;44:1010–20. https://doi.org/10.1016/j.ijhydene.2018.10.227.

[38] Petitpas G, Moreno-Blanco J, Espinosa-Loza F, Aceves SM. Rapid high density cryogenic pressure vessel filling to 345 bar with a liquid hydrogen pump. Int J Hydrog Energy 2018;43:19547–58. https://doi.org/10.1016/j.ijhydene.2018.08.139.

[39] Moreno-Blanco JC, Elizalde-Blancas F, Gallegos-Muñoz A, Aceves SM. The potential for avoiding hydrogen release from cryogenic pressure vessels after vacuum insulation failure. Int J Hydrog Energy 2018;43:8170–8. https://doi.org/10.1016/j.ijhydene.2018.02.150.

[40] Aceves SM, Berry GD, Rambach GD. Insulated pressure vessels for hydrogen storage on vehicles. Int J Hydrog Energy 1998;23:583–91. https://doi.org/10.1016/S0360-3199(97)00079-7.

[41] Aceves SM, Petitpas G, Espinosa-Loza F, Matthews MJ, Ledesma-Orozco E. Safe, long range, inexpensive and rapidly refueable hydrogen vehicles with cryogenic pressure vessels. Int J Hydrog Energy 2013;38:2480–9. https://doi.org/10.1016/j.ijhydene.2012.11.123.

[42] Aceves SM, Espinosa-Loza F, Ledesma-Orozco E, Ross TO, Weisberg AH, Brunner TC, et al. High-density automotive hydrogen storage with cryogenic capable pressure vessels. Int J Hydrog Energy 2010;35:1219–26. https://doi.org/10.1016/j.ijhydene.2009.11.069.

[43] Ahluwalia RK, Peng JK. Dynamics of cryogenic hydrogen storage in insulated pressure vessels for automotive applications. Int J Hydrog Energy 2008;33:4622–33. https://doi.org/10.1016/j.ijhydene.2008.05.090.

[44] Ahluwalia RK, Hua TQ, Peng J-K, Lasher S, McKenney K, Sinha J, et al. Technical assessment of cryo-compressed hydrogen storage tank systems for automotive applications. Int J Hydrog Energy 2010;35:4171–84. https://doi.org/10.1016/j.ijhydene.2010.02.074.

[45] Peng JK, Ahluwalia RK. Enhanced dormancy due to para-to-ortho hydrogen conversion in insulated cryogenic pressure vessels for automotive applications. Int J Hydrog Energy 2013;38:13664–72. https://doi.org/10.1016/j.ijhydene.2013.08.039.

[46] Ahluwalia RK, Peng JK, Roh HS, Hua TQ, Houchins C, James BD. Supercritical cryo-compressed hydrogen storage for fuel cell electric buses. Int J Hydrog Energy 2018;43:10215–31. https://doi.org/10.1016/j.ijhydene.2018.04.113.

[47] Moreno-Blanco J, Petitpas G, Espinosa-Loza F, Elizalde-Blancas F, Martinez-Frias J, Aceves SM. The storage performance of automotive cryo-compressed hydrogen vessels. Int J Hydrog Energy 2019;44:16841–51. https://doi.org/10.1016/j.ijhydene.2019.04.189.

[48] Ahluwalia RK, Peng J-K, Roh H-S, Papadias D, Wang X, Aceves SM. Liquid hydrogen storage system for heavy duty trucks: capacity, dormancy, refueling, and discharge. Int J Hydrog Energy 2023;48:34120–31. https://doi.org/10.1016/j.ijhydene.2023.05.113.

[49] Petitpas G, Aceves SM, Matthews MJ, Smith JR. Para-H2 to ortho-H2 conversion in a full-scale automotive cryogenic pressurized hydrogen storage up to 345 bar. Int J Hydrog Energy 2014;39:6533–47. https://doi.org/10.1016/j.ijhydene.2014.01.205.

[50] Mann D. LNG materials and fluids: technical report. National Bureau of Standards Cryogenics Division; 1977.

[51] NIST. Material properties: G-10 CR (fiberglass epoxy). n.d. https://trc.nist.gov/cryogenics/materials/. [Accessed 30 November 2023].

[52] Estey PN, Lewis DH, Connor M. Prediction of a propellant tank pressure history using state space methods. J Spacecr Rockets 1983;20:49–54. https://doi.org/10.2514/3.28355.

[53] Osipov VV, Daigle MJ, Muratov CB, Foygel M, Smelyanskiy VN, Watson MD. Dynamical model of rocket propellant loading with liquid hydrogen. J Spacecr Rockets 2011;48:987–98. https://doi.org/10.2514/1.52587.

[54] Petitpas G. Simulation of boil-off losses during transfer at a LH2 based hydrogen refueling station. Int J Hydrog Energy 2018;43:21451–63. https://doi.org/10.1016/j.ijhydene.2018.09.132.

[55] Kuehn TH, Goldstein RJ. An experimental study of natural convection heat transfer in concentric and eccentric horizontal cylindrical annuli. J Heat Transf 1978;100:635–40. https://doi.org/10.1115/1.3450869.

[56] Apostolou D, Xydis G. A literature review on hydrogen refuelling stations and infrastructure: current status and future prospects. Renew Sustain Energy Rev 2019;113:109292. https://doi.org/10.1016/j.rser.2019.109292.

[57] Bauer A, Mayer T, Semmel M, Guerrero Morales MA, Wind J. Energetic evaluation of hydrogen refueling stations with liquid or gaseous stored hydrogen. Int J Hydrog Energy 2019;44:6795–812. https://doi.org/10.1016/j.ijhydene.2019.01.087.

[58] Molkov V, Dadashzadeh M, Makarov D. Physical model of onboard hydrogen storage tank thermal behaviour during fuelling. Int J Hydrog Energy 2019;44:4374–84. https://doi.org/10.1016/j.ijhydene.2018.12.115.

[59] Kuroki T, Sakoda N, Shinzato K, Monde M, Takata Y. Dynamic simulation for optimal hydrogen refueling method to fuel cell vehicle tanks. Int J Hydrog Energy 2018;43:5714–21. https://doi.org/10.1016/j.ijhydene.2018.01.111.

[60] Kuroki T, Nagasawa K, Peters M, Leighton D, Kurtz J, Sakoda N, et al. Thermodynamic modeling of hydrogen fueling process from high-pressure storage tank to vehicle tank. Int J Hydrog Energy 2021;46:22004–17. https://doi.org/10.1016/j.ijhydene.2021.04.037.

[61] Caponi R, Monforti Ferrario A, Bocci E, Valenti G, Della Pietra M. Thermodynamic modeling of hydrogen refueling for heavy-duty fuel cell buses and comparison with aggregated real data. Int J Hydrog Energy 2021;46:18630–43. https://doi.org/10.1016/j.ijhydene.2021.02.224.

[62] He M, Lv C, Gong L, Wu J, Zhu W, Zhang Y, et al. The design and optimization of a cryogenic compressed hydrogen refueling process. Int J Hydrog Energy 2021;46:29391–9. https://doi.org/10.1016/j.ijhydene.2020.11.061.

[63] Elgowainy A, Reddi K, Lee D-Y, Rustagi N, Gupta E. Techno-economic and thermodynamic analysis of pre-cooling systems at gaseous hydrogen refueling stations. Int J Hydrog Energy 2017;42:29067–79. https://doi.org/10.1016/j.ijhydene.2017.09.087.

[64] Society of Automotive Engineers. Fueling protocols for light duty gaseous hydrogen surface vehicles. SAE International; 2020.

[65] Kanda M, Matsumoto K, Yamaguchi S. Heat transfer through multi-layer insulation (MLI). Physica C, Supercond Appl 2021;583:1353799. https://doi.org/10.1016/j.physc.2020.1353799.

[66] Clean Energy Partnership. White paper requirements specification: subcooled liquid hydrogen fueling interface for ground vehicles. https://cleanenergypartnership.de/en/truck-refuelling-paths. [Accessed 30 November 2023]; 2021.

[67] Sand M, Skeie RB, Sandstad M, Krishnan S, Myhre G, Bryant H, et al. A multi-model assessment of the global warming potential of hydrogen. Commun Earth Environ 2023;4. https://doi.org/10.1038/s43247-023-00857-8.

[68] Schäfer S, Maus S. Technology pitch: subcooled liquid hydrogen (slh2). https://www.now-gmbh.de/wp-content/uploads/2021/05/Heavy-Duty-Event-Subcooled-Liquid-Hydrogen-sLH2-Schaefer-Linde-Maus-Daimler.pdf. [Accessed 30 November 2023]; 21 April 2021.

[69] Yang M, Hu S, Yang F, Xu L, Bu Y, Yuan D. On-board liquid hydrogen cold energy utilization system for a heavy-duty fuel cell hybrid truck. World Electr Veh J 2021;12:136. https://doi.org/10.3390/wevj12030136.

[70] Schmidt A. Technical thermodynamics for engineers: basics and applications, Springer eBooks engineering. 1st ed. 2019 ed. Cham: Springer; 2019.

[71] Span R. Multiparameter equations of state: an accurate source of thermodynamic property data. Berlin and Heidelberg: Springer; 2000.

[72] Thorade M, Saadat A. Partial derivatives of thermodynamic state properties for dynamic simulation. Environ Earth Sci 2013;70:3497–503. https://doi.org/10.1007/s12665-013-2394-z.